

# Decay and renormalization of a Higgs amplitude mode in a quasi-two-dimensional antiferromagnet\*

Seung-Hwan Do,<sup>1,†</sup> Hao Zhang,<sup>1,2,†</sup> Travis J. Williams,<sup>3</sup> Tao Hong,<sup>3</sup> V. Ovidiu Garlea,<sup>3</sup> Tae-Hwan Jang,<sup>4</sup> Sang-Wook Cheong,<sup>4,5</sup> Jae-Hoon Park,<sup>4,6</sup> Cristian D. Batista,<sup>2</sup> and Andrew D. Christianson<sup>1</sup>

<sup>1</sup>Materials Science and Technology Division, Oak Ridge National Laboratory, Oak Ridge, Tennessee 37831, USA<sup>‡</sup>

<sup>2</sup>Department of Physics and Astronomy, University of Tennessee, Knoxville, Tennessee 37996, USA

<sup>3</sup>Neutron Scattering Division, Oak Ridge National Laboratory, Oak Ridge, Tennessee 37831, USA

<sup>4</sup>MPPHC-CPM, Max Planck POSTECH/Korea Research Initiative, Pohang 37673, Republic of Korea

<sup>5</sup>Rutgers Center for Emergent Materials and Department of Physics and Astronomy,

Rutgers University, Piscataway, New Jersey 08854, USA

<sup>6</sup>Department of Physics, Pohang University of Science and Technology, 37673, Republic of Korea

(Dated: September 8, 2022)

We study the emergence, decay and renormalization of the longitudinal (Higgs) mode of a spin one easy-plane antiferromagnet near the continuous quantum phase transition into a quantum paramagnet (QPM). Our inelastic neutron scattering measurements demonstrate that  $\text{Ba}_2\text{FeSi}_2\text{O}_7$  is a quasi-two-dimensional antiferromagnet in close proximity to a quantum critical point. While a longitudinal mode is clearly observed throughout the Brillouin zone, the decay of the mode is particularly pronounced at the zone center. This phenomenon, as well as the corresponding renormalization of the transverse and longitudinal mode dispersions, are well described by a generalized linear spin-wave theory with one-loop corrections.

## I. INTRODUCTION

An ongoing challenge in the study of quantum material, is to incorporate quantum effects that are not captured by the simplest semiclassical approaches. One of the strongest signatures of quantum behavior is the spontaneous quasiparticle decay in interacting bosonic systems, as observed in superfluids [1–3] and quantum magnets [4–8]. In the latter case, this many body effect is typically enhanced near quantum critical points that signal a continuous quantum phase transition between two different phases. For these reasons, spontaneous magnon decay has been studied both theoretically and experimentally in a growing number of lattice geometries and model systems with large quantum fluctuations [9, 10]. Studies in triangular lattice materials have revealed that the strong decay processes are accompanied by a significant renormalization of the overall spectra [11–16]. This spectral renormalization has an important implication, namely that the renormalized single-magnon dispersion provides a stringent test for theories that attempt to reproduce measured effects of magnon decay. In other

words, approaches that do not fully incorporate these many-body effects will not yield correct values of the interaction parameters extracted from fits of inelastic neutron scattering data.

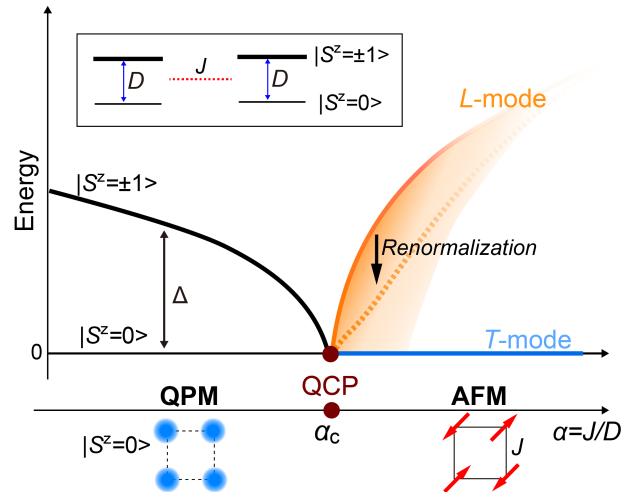


FIG. 1. Schematic phase diagram illustrating the  $O(2)$  quantum critical point (QCP) between the antiferromagnetic (AFM) state and the quantum paramagnet (QPM) as a function of  $J/D$  ( $J$  is a Heisenberg exchange and  $D$  is a easy-plane single-ion anisotropy). The low-energy excitations of the QPM are two degenerate  $S^z=\pm 1$  modes (black line) with a gap,  $\Delta$ , which closes at the QCP. The spontaneous  $U(1)$  symmetry breaking leads to a gapless magnon or transverse mode ( $T$ -mode), indicated with a blue line, which is accompanied by a gapped longitudinal mode ( $L$ -mode) indicated with the orange line. Near the QCP, the energy and the lifetime of the  $L$ -mode are strongly renormalized (dashed orange line) due to the decay into the continuum of two transverse modes (shaded orange region).

\* This manuscript has been authored by UT-Battelle, LLC under Contract No. DE-AC05-00OR22725 with the U.S. Department of Energy. The United States Government retains and the publisher, by accepting the article for publication, acknowledges that the United States Government retains a non-exclusive, paid-up, irrevocable, world-wide license to publish or reproduce the published form of this manuscript, or allow others to do so, for United States Government purposes. The Department of Energy will provide public access to these results of federally sponsored research in accordance with the DOE Public Access Plan (<http://energy.gov/downloads/doe-public-access-plan>).

† These authors contributed equally.

‡ doh1@ornl.gov

The objective of this paper is to explore these ideas for the case of interacting longitudinal and transverse modes for easy-plane quantum magnets. Phase transitions of easy-plane quantum magnets can be driven by either fluctuations of the phase or the amplitude of the order parameter [17]. The phase fluctuations are the transverse modes of the order parameter (Goldstone modes in the long wavelength limit), whereas amplitude fluctuations correspond to the longitudinal modes. Due to the gapless nature of the Goldstone transverse modes, the longitudinal or “Higgs” mode is kinematically allowed to decay into two transverse modes. This decay becomes more significant in low-dimensional systems. Indeed, the longitudinal mode in 2D antiferromagnets was originally assumed to be overdamped due to an infrared divergence of the imaginary part of the longitudinal susceptibility [18, 19]. However, more recent theoretical work predicted that the longitudinal peak should remain visible even in 2D [20–23]. One aspect of this problem, which has not been emphasized in previous works, is that the rather strong decay of the longitudinal mode is accompanied by a significant renormalization of the gap and the dispersion of the modes. As noted above, this additional many-body effect provides a hard test for theories that attempt to reproduce the measured decay of the Higgs mode.

To put the basic physics on a firm footing, we focus on the two-dimensional Heisenberg square lattice (2dHSL) with effective  $S=1$  with an antiferromagnetic exchange coupling ( $J$ ) and a strong easy-plane single-ion anisotropy ( $D$ ). In this case,  $\alpha = J/D$  can be viewed as a tuning parameter that can be used to drive a system from a quantum paramagnet (QPM) to an antiferromagnet (AFM) with an intervening QCP as shown in the Fig. 1. Near the QCP, spontaneous symmetry breaking produces two transverse Goldstone modes and a longitudinal Higgs mode. The longitudinal mode is unstable with respect to decay into a pair of transverse modes resulting in an intrinsic line-broadening [9, 24].

In this paper we reveal and explain the physics of interacting transverse and longitudinal modes using experimental inelastic neutron scattering studies along with the development of a theory for studying this problem. Our comprehensive inelastic neutron scattering measurements of a single crystal of  $\text{Ba}_2\text{FeSi}_2\text{O}_7$  (see Sec. III) uncover a well-defined longitudinal mode. The energy dependence and line-broadening of the mode exhibit strong wave vector dependence throughout the Brillouin zone. As explained in Sec. IV, we use an SU(3) spin wave calculation [25–27] to compute the low-energy excitation spectrum of the effective low-energy spin  $S = 1$  model that is derived in Sec. II. More importantly, in Sec. V we demonstrate that the generalization of the well-known  $1/S$  expansion of the SU(2) spin wave theory [28, 29] is simply a loop expansion [30] of the SU( $N$ ) spin wave theory for an arbitrary value of  $N$  (including  $N = 2$ ). By including one loop corrections, we compute the broadening of the Higgs mode due to the decay into two transverse modes,

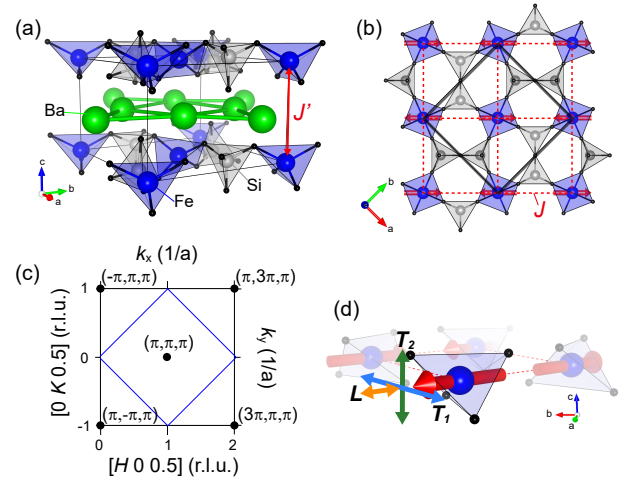


FIG. 2. (a) Crystal structure of  $\text{Ba}_2\text{FeSi}_2\text{O}_7$ . Ba atoms separate layers composed of  $\text{FeSi}_2\text{O}_7$ , rendering a quasi-two-dimensional structure. (b) In the  $\text{FeSi}_2\text{O}_7$  layer,  $\text{FeO}_4$  tetrahedra are connected via  $\text{SiO}_4$  polyhedra, and the adjacent two  $\text{Fe}^{2+}$  atoms are exchange coupled by two oxygen ligands. The red dashed line indicates the exchange pathway  $J$  within two-dimensional square spin network. The interlayer coupling  $J'$  is found here to be much weaker than  $J$ . Red arrows indicate the moment direction in the collinear AFM phase as determined in Ref. [32]. The black solid line indicates the chemical unit cell. (c)  $HK$ -reciprocal space with  $L=0.5$  in the tetragonal structure ( $P\bar{4}2_1m$ ). The blue solid line and the black circle indicate the Brillouin zone and zone center, respectively. The coordinates  $(H\ K\ L)$  of the reciprocal lattice of the origin lattice are related to  $(k_x\ k_y\ k_z)$  of the magnetic lattice formed by the  $\text{Fe}^{2+}$  atoms through  $k_x = 2\pi(H - K)$ ,  $k_y = 2\pi(H + K)$ , and  $k_z = 2\pi L$ . (d) Illustration of the spin fluctuation modes.  $T_1$  and  $T_2$  indicate transverse fluctuation in the  $ab$ -plane and out-of the plane, respectively.  $L$  indicates longitudinal fluctuation of spin.

which is accompanied by a large renormalization of the gap and the dispersion of the mode. We further show that not including the one-loop corrections in the generalized linear spin wave theory results in Hamiltonian parameters that place the exact ground state of the spin Hamiltonian for  $\text{Ba}_2\text{FeSi}_2\text{O}_7$  on the nonmagnetic side of the QCP—contrary to experimental fact—providing a dramatic demonstration of the importance of renormalization effects [31]. As expected, the Goldstone mode of the theory, which is dictated by the  $U(1)$  symmetry of the effective  $S = 1$  spin model, is preserved by the one-loop correction only when all of the one-loop diagrams are included. The fact that the one-loop correction can simultaneously account for the real and imaginary part of the self-energy of the amplitude mode, as well as of the renormalization the transverse mode dispersion, confirms that  $\text{Ba}_2\text{FeSi}_2\text{O}_7$  is an ideal platform for studying many-body effects in the proximity of an  $O(2)$  QCP in  $D = 3 + 1$  dimensions.

## II. MODEL MATERIAL

Figure 2 (a) illustrates the crystal structure of  $\text{Ba}_2\text{FeSi}_2\text{O}_7$  comprising layers of  $\text{FeSi}_2\text{O}_7$  separated by Ba atoms. As shown in Fig. 2 (b), the  $\text{FeO}_4$  tetrahedra of the  $\text{FeSi}_2\text{O}_7$  layer are connected via  $\text{SiO}_4$  polyhedra and the two adjacent  $\text{Fe}^{2+}$  atoms are coupled through the super-exchange interaction,  $J$ , that is mediated by the two oxygen ligands (red dashed line in Fig. 2 (b)). The resulting square lattice of magnetic moments are vertically stacked along the  $c$ -axis, leading to a quasi-two-dimensional simple tetragonal spin-lattice.

Appendix B includes a detailed description of the single-ion state of the  $\text{Fe}^{2+}$  ion. The combination of a relatively large spin-orbit coupling ( $\lambda \sim 20$  meV) and a dominant tetrahedral crystal field ( $\Delta_{Td}$ ), splits the free-ion levels,  $^5D$  ( $L=2, S=2$ ), into several multiplets. The lowest energy  $S=2$  multiplet has a significant orbital character due to the finite spin-orbit coupling, that combined with the tetragonal distortion ( $\delta_{\text{Tetra}}$ ) by large compression of the  $\text{FeO}_4$  tetrahedra leads to a rather strong easy-plane single-ion anisotropy  $D$  [32, 33]. The five  $S=2$  energy levels are then split into a singlet  $S^z=0$  ground state and two excited  $S^z=\pm 1$  and  $S^z=\pm 2$  doublets with energies  $D$  and  $4D$ , respectively (see Fig. 9 (a)). Because the gap  $D$  of the  $S^z=\pm 1$  doublet is four times smaller than the gap of the  $S^z=\pm 2$  doublet and the dominant super-exchange interaction  $J$  is smaller than  $D/4$  in  $\text{Ba}_2\text{FeSi}_2\text{O}_7$ , the low-energy spectrum is well captured by projecting the  $S=2$  spin Hamiltonian into the  $S^z=0$  and  $S^z=\pm 1$  low-energy states.

The resultant  $S=1$  effective spin Hamiltonian describes the competition between a QPM ( $J \ll D$ ) with each spin of the lattice having dominant  $S^z=0$  character, and a collinear AFM state ( $\alpha = J/D > \alpha_c$ ) with staggered magnetization in the  $ab$ -plane (see Fig. 2 (b)).  $\text{Ba}_2\text{FeSi}_2\text{O}_7$  turns out to be on the antiferromagnetic side with a Néel temperature  $T_N=5.2$  K [32]. Below  $T_N$ , the spins magnetically order with propagation vector  $\mathbf{Q}_m=(1\ 0\ 0.5)$ , corresponding to  $(\pi, \pi, \pi)$  as shown in Fig. 2 (c). The magnetic moments are highly confined in the  $ab$ -plane due to easy-plane anisotropy, giving rise to the magnetic structure shown in Fig. 2 (b). A neutron diffraction study on a powder sample revealed a significantly reduced ordered moment of  $2.6\ \mu_B$ , which is only 65% of the full moment of  $4\ \mu_B$  ( $g=2$ ) expected for an  $S=2$  spin [32], supporting an effective  $S=1$  picture. Additionally, as described in further detail below, our analysis confirms that  $\alpha = J/D \sim 0.184$  is close to the critical value,  $\alpha_c^{2D}=0.18$  and  $\alpha_c^{3D}=0.1$  for two-dimensional and three-dimensional respectively, obtained from quantum Monte Carlo simulations [27].

The spin excitations of  $\text{Ba}_2\text{FeSi}_2\text{O}_7$  are generically described by an antiferromagnetic  $S=2$  spin Hamiltonian on a simple tetragonal lattice:

$$\begin{aligned} \mathcal{H} = & J \sum_{\langle \mathbf{r}, \mathbf{r}' \rangle} [S_{\mathbf{r}}^x S_{\mathbf{r}'}^x + S_{\mathbf{r}}^y S_{\mathbf{r}'}^y + \Delta S_{\mathbf{r}}^z S_{\mathbf{r}'}^z] \\ & + J' \sum_{\langle\langle \mathbf{r}, \mathbf{r}' \rangle\rangle} [S_{\mathbf{r}}^x S_{\mathbf{r}'}^x + S_{\mathbf{r}}^y S_{\mathbf{r}'}^y + \Delta' S_{\mathbf{r}}^z S_{\mathbf{r}'}^z] \\ & + D \sum_{\mathbf{r}} (S_{\mathbf{r}}^z)^2. \end{aligned} \quad (1)$$

The bracket  $\langle \mathbf{r}, \mathbf{r}' \rangle$  ( $\langle\langle \mathbf{r}, \mathbf{r}' \rangle\rangle$ ) indicates that the sum runs over intralayer (interlayer) nearest-neighbor spins with isotropic super-exchange interaction  $J(J')$ .  $\Delta$  ( $\Delta'$ ) is the intralayer (interlayer) uniaxial anisotropy and the last term represents the easy-plane single-ion anisotropy ( $D > 0$ ).

In the large  $D/J$  limit, the  $S^z = \pm 2$  doublet is separated from the  $S^z = \pm 1$  doublet by an energy gap  $3D$ . The low-energy subspace of magnetic excitations can then be further reduced by projecting out the  $S^z = \pm 2$  doublet. The reduced low-energy Hamiltonian  $\mathcal{H}_{\text{eff}}$  results from projecting  $\mathcal{H}$  onto the low-energy subspace  $\mathcal{S}$  spanned by the triplet of states with  $S^z = 0, \pm 1$ :  $\mathcal{H}_{\text{eff}} = \mathcal{P}_{\mathcal{S}} \mathcal{H} \mathcal{P}_{\mathcal{S}}$ . The resulting effective spin  $S=1$  Hamiltonian is

$$\begin{aligned} \mathcal{H}_{\text{eff}} = & \tilde{J} \sum_{\langle \mathbf{r}, \mathbf{r}' \rangle} [S_{\mathbf{r}}^x S_{\mathbf{r}'}^x + S_{\mathbf{r}}^y S_{\mathbf{r}'}^y + \tilde{\Delta} S_{\mathbf{r}}^z S_{\mathbf{r}'}^z] \\ & + \tilde{J}' \sum_{\langle\langle \mathbf{r}, \mathbf{r}' \rangle\rangle} [S_{\mathbf{r}}^x S_{\mathbf{r}'}^x + S_{\mathbf{r}}^y S_{\mathbf{r}'}^y + \tilde{\Delta}' S_{\mathbf{r}}^z S_{\mathbf{r}'}^z] \\ & + \tilde{D} \sum_{\mathbf{r}} (S_{\mathbf{r}}^z)^2. \end{aligned} \quad (2)$$

with  $\tilde{J} = 3J$ ,  $\tilde{J}' = 3J'$ ,  $\tilde{\Delta} = \Delta/3$ ,  $\tilde{\Delta}' = \Delta'/3$  and  $\tilde{D} = D$ . As we will see below, this simple effective Hamiltonian can explain not only the in-plane antiferromagnetic ordering observed in  $\text{Ba}_2\text{FeSi}_2\text{O}_7$  (see Fig. 2 (b)), but also the spectra of quasi-particle excitations, including rather strong renormalization effects due to proximity to the QCP.

## III. INELASTIC NEUTRON SCATTERING

To investigate the spin excitation spectrum in  $\text{Ba}_2\text{FeSi}_2\text{O}_7$ , we performed inelastic neutron scattering using two instruments; the cold neutron triple-axis spectrometer (CTAX) at the High Flux Isotope Reactor, and the time-of-flight hybrid spectrometer (HYSPEC) at the Spallation Neutron Source at Oak Ridge National Laboratory [34] (see Appendix A for additional details). An overview of the inelastic neutron scattering results is presented in Fig. 3 through contour maps of the dynamic structure factor,  $S(\mathbf{Q}, \omega)$ , along  $[H, H, 0.5]$  and  $[H, 0, 0.5]$ . For both spectra, strongly dispersive spin excitations extending up to  $dE \sim 2.7$  meV are observed. Whereas the dispersion along  $L$ -direction is weak with a bandwidth of

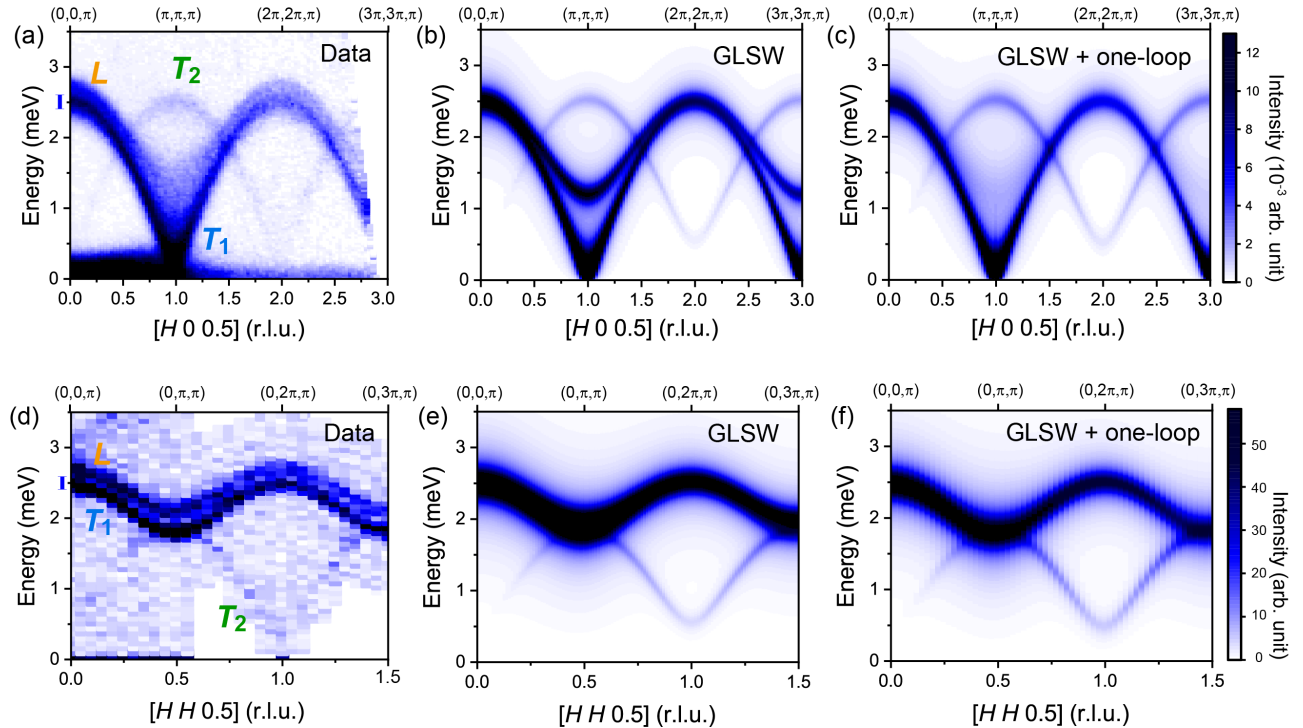


FIG. 3. (a) Contour map of the inelastic neutron scattering (INS) data as a function of energy and momentum transfer along the  $[H,0,0.5]$  direction measured at  $T=1.6$  K ( $< T_N$ ) using the HYSPEC time-of-flight spectrometer at SNS. (d) Contour map of the INS data as a function of energy and momentum transfer along  $[H,H,0.5]$  direction measured at  $T=1.4$  K ( $< T_N$ ) using the cold Neutron Triple-Axis spectrometer (CTAX) at HFIR. The instrumental resolutions at  $dE=2.5$  meV for each instrument are indicated with blue bars along the  $y$ -axis in (a) and (d). The two transverse modes and the longitudinal mode are labeled with  $T_1$ ,  $T_2$ , and  $L$ , respectively. (b),(c),(e), and (f) INS intensities calculated by the generalized linear spin wave theory (GLSWT) and GLSWT plus one-loop corrections (GLSWT+one-loop) with the parameter sets  $\mathcal{A}$  and  $\mathcal{B}$  given in Table. I, respectively. The instrumental resolution of HYSPEC and CTAX was modeled in the calculated spectra using a Lorentzian function.

$\sim 0.5$  meV (see Appendix D), which is expected for spin excitations in a quasi-two-dimensional spin system.

There are several distinct features in the inelastic neutron scattering data. An intense spin wave excitation emanates from the magnetic zone center (ZC),  $\mathbf{Q}=(1\ 0\ 0.5)$ , which arises due to the in-phase oscillation between  $\text{Fe}^{2+}$  spins in the plane. We refer to this mode as  $T_1$ . Along the  $[H,0,0.5]$  direction towards the zone boundary (ZB) at  $\mathbf{Q}=(0,0,0.5)$  the  $T_1$ -mode reaches its maximum energy of  $\sim 2.5$  meV. Another weak, but sharp mode, is visible along  $[H,0,0.5]$  with an energy of 2.5 meV at the ZC. This mode is due to out-of-plane fluctuations (see Fig. 2 (d)) [35]. The finite value of energy at the ZC is due to the presence of easy-plane single-ion anisotropy. We refer to this mode as  $T_2$ .

The  $T_1$  and  $T_2$  transverse magnon modes are also observed along the  $[H,H,0.5]$  direction in Fig. 3 (d). Noticeably, an additional sharp mode is observed at the top of the  $T_1$ -mode. This mode is visible along the entire Brillouin zone boundary. We refer to this additional mode as ‘ $L$ ’-mode. The  $L$ -mode is visible in the spectra along  $[H,0,0.5]$  as well, however, the mode exhibits dramatic line-broadening near ZC. To demonstrate more clearly the  $\mathbf{Q}$ -dependence of the modes, Fig. 4 shows cuts at

constant momentum transfers for multiple points along  $[H,0,0.5]$  and  $[H,H,0.5]$ . Two pronounced peaks, corresponding to the  $T_1$  and  $L$  modes, remain sharp along the ZB (Fig. 4 (b)). As already noted, the situation is very different near the ZC where the  $L$  mode is significantly broadened (Fig. 4 (a)). We note that the  $L$ -mode remains a broad peak near the ZC, rather than a featureless excitation. To investigate the extent of the broadening effect, Gaussian line shapes for the  $T_1$ ,  $T_2$ , and  $L$  modes were fit to the individual cuts in Fig. 4. The line widths obtained from the fits are displayed in Fig. 7 (a)-(d). These results reveal that the  $L$ -mode is factor of three broader than the instrumental resolution at the ZC (see Fig. 4 (a)), whereas it has comparable line width to instrumental resolution near the ZB.

#### IV. GENERALIZED SPIN WAVES

In this section we introduce a generalized SU(3) spin wave calculation [25–27], which is required to capture the two low-energy (longitudinal and transverse) modes of  $\text{Ba}_2\text{FeSi}_2\text{O}_7$ . It is clear that a linear treatment is not enough to capture the decay of the longitudinal mode

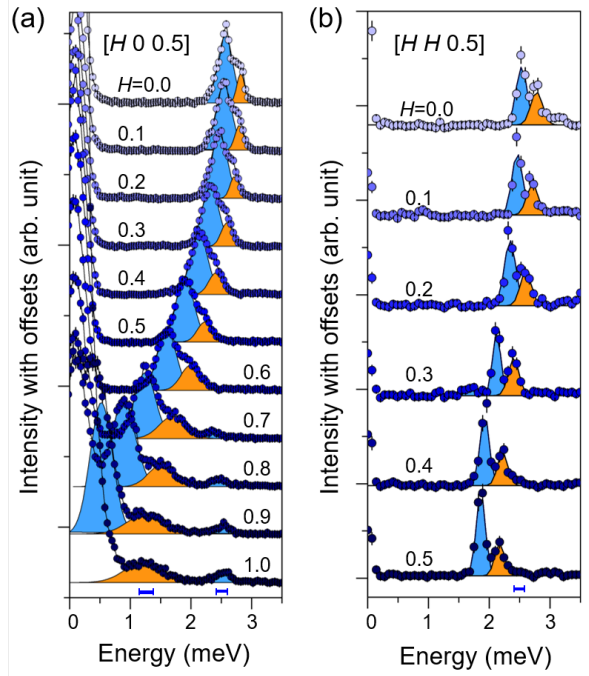


FIG. 4. (a) Constant momentum cuts at points along the  $[H, 0, 0.5]$  direction measured using HYSPEC at SNS, integrated over  $H = [H-0.05, H+0.05]$  at selected  $H$ ,  $K = [-0.1, 0.1]$ , and  $L = [0.4, 0.6]$ . (b) Constant momentum cuts at points along the  $[H, H, 0.5]$  direction measured using CTAX at HFIR. Blue bars at the bottom of the panels indicate the instrumental resolutions for HYSPEC and CTAX at the proximate energy transfers. The blue and orange shaded regions are the results of fitting Gaussian line shapes to transverse ( $T_1, T_2$ ) and longitudinal ( $L$ ) modes, respectively.

into two transverse modes. Consequently, the main aim of the section is to lay the groundwork for introducing the loop expansion (generalization of the  $1/S$  expansion) that we explain in Sec. V.

### A. SU(3) Formalism

To account for the transverse and longitudinal modes revealed by the INS experiment, the usual SU(2) spin-wave theory (SWT) must be generalized to SU(3), [26] by introducing the SU(3) Schwinger boson representation of the spin operators  $S_{\mathbf{r}}^{\nu} = \mathbf{b}_{\mathbf{r}}^{\dagger} \mathcal{S}^{\nu} \mathbf{b}_{\mathbf{r}}$ , where  $\mathbf{b}_{\mathbf{r}} = (b_{\mathbf{r},+1}, b_{\mathbf{r},-1}, b_{\mathbf{r},0})^T$ ,

$$\mathcal{S}^x = \frac{1}{\sqrt{2}}(\lambda_4 + \lambda_6), \quad \mathcal{S}^y = \frac{1}{\sqrt{2}}(\lambda_5 - \lambda_7), \quad \mathcal{S}^z = \lambda_3, \quad (3)$$

$\lambda_i$  are the Gel-Mann matrices and the Schwinger boson operators satisfy the local constraint

$$\sum_{m=\pm 1,0} b_{\mathbf{r},m}^{\dagger} b_{\mathbf{r},m} = M = 1. \quad (4)$$

The magnetically ordered state of  $\text{Ba}_2\text{FeSi}_2\text{O}_7$  can be approximated by a product (mean-field) state of normalized SU(3) coherent states

$$|\psi_{\mathbf{r}}\rangle = \cos \theta |0\rangle + (\sin \theta \cos \phi |1\rangle + \sin \theta \sin \phi | -1\rangle) e^{i\mathbf{Q}_m \cdot \mathbf{r}}, \quad (5)$$

where  $\mathbf{Q}_m = (\pi, \pi, \pi)$  ((1, 0, 0.5) in the chemical lattice) is the AFM ordering wave vector. Although a general SU(3) coherent state is a parameterized by 4 independent parameters (not including the irrelevant global phase), the two independent parameters  $\theta$  and  $\phi$  are enough to describe the collinear order under consideration. The three basis states  $|m\rangle$  ( $m = 0, \pm 1$ ) are represented by creating a boson with quantum number  $m$  from the vacuum:  $|m\rangle = b_{\mathbf{r},m}^{\dagger} |\emptyset\rangle$ .

As in the usual spin wave theory, we introduce an SU(3) transformation that rotates the boson operators,  $\tilde{\mathbf{b}}_{\mathbf{r}} = U_{\mathbf{r}} \mathbf{b}_{\mathbf{r}}$ , to a local basis that includes the coherent SU(3) state (5) as one of its three elements. This local transformation allows us to align the quantization axis with the direction of the local SU(3) order parameter. The spatial dependence of  $U_{\mathbf{r}}$  can be removed by working in a twisted frame, where the original AFM order becomes a FM one. This can be done by rotating the spin reference frame of one of the two sublattices of the tetragonal lattice by an angle  $\pi$  along the  $z$ -axis:  $S_{\mathbf{r}}^z \rightarrow S_{\mathbf{r}}^z$ , and  $S_{\mathbf{r}}^{x,y} \rightarrow -S_{\mathbf{r}}^{x,y}$ . In the new reference frame, the effective Hamiltonian (2) becomes

$$\tilde{\mathcal{H}}_{\text{eff}} = \tilde{J} \sum_{\langle \mathbf{r}, \mathbf{r}' \rangle, \nu} a_{\nu} S_{\mathbf{r}}^{\nu} S_{\mathbf{r}'}^{\nu} + \tilde{J}' \sum_{\langle \mathbf{r}, \mathbf{r}' \rangle, \nu} b_{\nu} S_{\mathbf{r}}^{\nu} S_{\mathbf{r}'}^{\nu} + \tilde{D} \sum_{\mathbf{r}} (S_{\mathbf{r}}^z)^2, \quad (6)$$

where  $a_x = a_y = b_x = b_y = -1$ ,  $a_z = \tilde{\Delta}$  and  $b_z = \tilde{\Delta}'$ . In the twisted frame, the SU(3) transformation reads

$$U = \begin{pmatrix} -\sin \phi & \cos \phi & 0 \\ \cos \theta \cos \phi & \cos \theta \sin \phi & -\sin \theta \\ \sin \theta \cos \phi & \sin \theta \sin \phi & \cos \theta \end{pmatrix}. \quad (7)$$

The bosonic representation of  $\tilde{\mathcal{H}}_{\text{eff}}$  is

$$\begin{aligned} \tilde{\mathcal{H}}_{\text{eff}} = & \tilde{J} \sum_{\langle \mathbf{r}, \mathbf{r}' \rangle, \nu} a_{\nu} \tilde{\mathbf{b}}_{\mathbf{r}}^{\dagger} \tilde{\mathcal{S}}^{\nu} \tilde{\mathbf{b}}_{\mathbf{r}} \tilde{\mathbf{b}}_{\mathbf{r}'}^{\dagger} \tilde{\mathcal{S}}^{\nu} \tilde{\mathbf{b}}_{\mathbf{r}'} \\ & + \tilde{J}' \sum_{\langle \mathbf{r}, \mathbf{r}' \rangle, \nu} b_{\nu} \tilde{\mathbf{b}}_{\mathbf{r}}^{\dagger} \tilde{\mathcal{S}}^{\nu} \tilde{\mathbf{b}}_{\mathbf{r}} \tilde{\mathbf{b}}_{\mathbf{r}'}^{\dagger} \tilde{\mathcal{S}}^{\nu} \tilde{\mathbf{b}}_{\mathbf{r}'} \\ & + \tilde{D} \sum_{\mathbf{r}} (1 - \tilde{\mathbf{b}}_{\mathbf{r}}^{\dagger} \tilde{\mathcal{A}} \tilde{\mathbf{b}}_{\mathbf{r}}) \end{aligned} \quad (8)$$

where  $\tilde{\mathcal{S}}^{\nu} = U \mathcal{S}^{\nu} U^{\dagger}$ ,  $\tilde{\mathcal{A}} = U \mathcal{A} U^{\dagger}$ , and  $\mathcal{A}_{\alpha\beta} = \delta_{\alpha,0} \delta_{\beta,0}$ . Note that the unitary transformation (7) is chosen in such a way that the  $\tilde{\mathbf{b}}_{\mathbf{r},0}$  boson is macroscopically occupied, namely  $\langle \tilde{\mathbf{b}}_{\mathbf{r},0} \rangle = \langle \tilde{\mathbf{b}}_{\mathbf{r},0}^{\dagger} \rangle \simeq \sqrt{M}$ . According to the constraint (4),  $M = 1$  for the case of interest. However, we will keep using  $M$  because  $1/M$  is the parameter of the perturbative expansion that will be introduced below. Note that  $M = 2S$  for the usual SU(2) spin wave

theory. The main assumption behind the  $1/M$  expansion is that  $\langle \tilde{b}_{\mathbf{r},-1}^\dagger \tilde{b}_{\mathbf{r},-1} \rangle, \langle \tilde{b}_{\mathbf{r},+1}^\dagger \tilde{b}_{\mathbf{r},+1} \rangle \ll M$ . Under this assumption, we can expand the spin operators  $S^\mu$  and the quadrupolar operator  $(S^z)^2$  in powers of  $1/M$  (see Appendix E). The resulting expansion of  $\tilde{\mathcal{H}}_{\text{eff}}$  is

$$\tilde{\mathcal{H}}_{\text{eff}} = M^2 \mathcal{H}^{(0)} + M \mathcal{H}^{(2)} + M^{1/2} \mathcal{H}^{(3)} + M^0 \mathcal{H}^{(4)} + \mathcal{O}(M^{-1}), \quad (9)$$

where the linear term  $\mathcal{H}^{(1)}$  vanishes because the parameters  $\theta$  and  $\phi$  in Eq. (5) are determined by minimizing the mean field energy

$$\begin{aligned} \mathcal{H}^{(0)} &= (2\tilde{J}\tilde{\Delta} + \tilde{J}'\tilde{\Delta}') \sin^4 \theta \cos^2 2\phi \\ &- \frac{1}{2}(2\tilde{J} + \tilde{J}') \sin^2 2\theta(1 + \sin 2\phi) + \tilde{D} \sin^2 \theta. \end{aligned} \quad (10)$$

Since the AFM order is invariant under time reversal followed by one lattice translation, the states  $|S_z = \pm 1\rangle$  must have equal weight in the mean field state (5), implying that  $\phi = \pi/4$ . By minimizing  $\mathcal{H}^{(0)}$  with respect to  $\theta$ , we obtain

$$x \equiv \sin^2 \theta = \frac{1}{2} - \frac{\tilde{D}}{8(2\tilde{J} + \tilde{J}')}. \quad (11)$$

## B. Generalized linear spin-wave theory

The quadratic term  $\mathcal{H}^{(2)}$  represents the generalized linear spin wave (GLSW) Hamiltonian. After Fourier transforming the bosonic operators,

$$\tilde{b}_{\mathbf{r}\alpha} = \frac{1}{\sqrt{N_s}} \sum_{\mathbf{k}} \tilde{b}_{\mathbf{k}\alpha} e^{i\mathbf{k}\cdot\mathbf{r}}, \quad (12)$$

where  $N_s$  is the number of sites,  $\mathcal{H}^{(2)}$  can be brought into a compact form by introducing the Nambu spinor  $\tilde{b}_{\mathbf{k}} = (\tilde{b}_{\mathbf{k},+1}, \tilde{b}_{\mathbf{k},-1}, \tilde{b}_{-\mathbf{k},+1}^\dagger, \tilde{b}_{-\mathbf{k},-1}^\dagger)^T$ ,

$$\mathcal{H}^{(2)} = \sum_{\mathbf{k}} \sum_{\alpha, \beta = \pm 1} \tilde{b}_{\mathbf{k}}^\dagger \mathcal{H}^{(2)}(\mathbf{k}) \tilde{b}_{\mathbf{k}}, \quad (13)$$

where

$$\mathcal{H}^{(2)}(\mathbf{k}) = \begin{pmatrix} \Delta_{\alpha\beta}(\mathbf{k}) & \Lambda_{\alpha\beta}(\mathbf{k}) \\ \Lambda_{\beta\alpha}(\mathbf{k}) & \Delta_{\beta\alpha}(\mathbf{k}) \end{pmatrix}. \quad (14)$$

The matrix elements are

$$\begin{aligned} \Delta_{\alpha\beta}(\mathbf{k}) &= \sum_{\nu} [(2a_{\nu}\tilde{J} + b_{\nu}\tilde{J}')(\tilde{\mathcal{S}}_{\alpha\beta}^{\nu}\tilde{\mathcal{S}}_{00}^{\nu} - (\tilde{\mathcal{S}}_{00}^{\nu})^2\delta_{\alpha\beta}) \\ &+ (\tilde{J}a_{\nu} \sum_{\nu'=x,y} \cos k_{\nu'} + \tilde{J}'b_{\nu} \cos k_z)\tilde{\mathcal{S}}_{\alpha 0}^{\nu}\tilde{\mathcal{S}}_{0\beta}^{\nu}] \\ &- \frac{\tilde{D}}{2}(\tilde{\mathcal{A}}_{\alpha\beta} - \tilde{\mathcal{A}}_{00}\delta_{\alpha\beta}), \end{aligned} \quad (15)$$

$$\Lambda_{\alpha\beta}(\mathbf{k}) = \sum_{\nu} \tilde{\mathcal{S}}_{\alpha 0}^{\nu}\tilde{\mathcal{S}}_{\beta 0}^{\nu} [\tilde{J}a_{\nu} \sum_{\nu'=x,y} \cos k_{\nu'} + \tilde{J}'b_{\nu} \cos k_z]. \quad (16)$$

The collinear mean-field state (5) remains invariant under the U(1) symmetry group of global spin rotations along the direction of the ordered moments (local  $\tilde{z}$ -axis). The bosonic operator  $\tilde{b}_{+1}^\dagger$  picks up minus sign under a  $\pi$ -rotation along the local  $\tilde{z}$ -axis because it creates the state with  $\tilde{S}^z = -1$ . In contrast, the bosonic operator  $\tilde{b}_{-1}^\dagger$  remains invariant because it creates the state with  $\tilde{S}^z = 0$ . This symmetry analysis implies that the  $\tilde{b}_{+1}$  and  $\tilde{b}_{-1}$  bosons must be decoupled in  $\mathcal{H}^{(2)}$  because a non-vanishing hybridization term would otherwise break this U(1) symmetry:

$$\mathcal{H}^{(2)} = \sum_{\mathbf{k}, \alpha = \pm 1} [A_{\mathbf{k}, \alpha} \tilde{b}_{\mathbf{k}, \alpha}^\dagger \tilde{b}_{\mathbf{k}, \alpha} - \frac{B_{\mathbf{k}, \alpha}}{2} (\tilde{b}_{-\mathbf{k}, \alpha} \tilde{b}_{\mathbf{k}, \alpha} + \tilde{b}_{\mathbf{k}, \alpha}^\dagger \tilde{b}_{-\mathbf{k}, \alpha}^\dagger)] \quad (17)$$

where  $\gamma_{\mathbf{k}}^{xy} = \cos(k_x) + \cos(k_y)$ ,  $\gamma_{\mathbf{k}}^z = \cos(k_z)$  and the expressions for  $A_{\mathbf{k}, \alpha}$  and  $B_{\mathbf{k}, \alpha}$  are given in Appendix E.

The diagonal form of  $\mathcal{H}^{(2)}$ ,

$$\mathcal{H}^{(2)} = \sum_{\mathbf{k}, \alpha = \pm 1} \omega_{\mathbf{k}, \alpha} \left( \beta_{\mathbf{k}, \alpha}^\dagger \beta_{\mathbf{k}, \alpha} + \frac{1}{2} \right) \quad (18)$$

is then obtained by applying an independent Bogoliubov transformation for each bosonic flavor,

$$\tilde{b}_{\mathbf{k}, \pm 1} = u_{\mathbf{k}, \pm 1} \beta_{\mathbf{k}, \pm 1} + v_{\mathbf{k}, \pm 1} \beta_{-\mathbf{k}, \pm 1}^\dagger, \quad (19)$$

with

$$\begin{aligned} u_{\mathbf{k}, \pm 1} &= \sqrt{\frac{1}{2} \left( \frac{|A_{\mathbf{k}, \pm 1}|}{\omega_{\mathbf{k}, \pm 1}} + 1 \right)}, \\ v_{\mathbf{k}, \pm 1} &= \frac{B_{\mathbf{k}, \pm 1}}{|B_{\mathbf{k}, \pm 1}|} \sqrt{\frac{1}{2} \left( \frac{|A_{\mathbf{k}, \pm 1}|}{\omega_{\mathbf{k}, \pm 1}} - 1 \right)}. \end{aligned} \quad (20)$$

The operators  $\beta_{\mathbf{k}, \pm 1}^\dagger$  create quasi-particles with energy

$$\omega_{\mathbf{k}, \pm 1} = \sqrt{A_{\mathbf{k}, \pm 1}^2 - B_{\mathbf{k}, \pm 1}^2}, \quad (21)$$

where  $\omega_{\mathbf{k},+1}(\omega_{\mathbf{k},-1})$  is the dispersion relation of the transverse (longitudinal) modes.

The neutron scattering intensity  $I(\mathbf{Q}, \omega)$  is related to the spin-spin correlation function through

$$\begin{aligned} I(\mathbf{Q}, \omega) &\propto f^2(\mathbf{Q}) \sum_{\mu, \nu} (\delta_{\mu\nu} - \frac{Q_{\mu}Q_{\nu}}{Q^2}) \\ &\frac{1}{2\pi N_s} \sum_{i,j}^{N_s} \int_{-\infty}^{+\infty} dt e^{i\omega t - i\mathbf{Q}\cdot(\mathbf{r}_i - \mathbf{r}_j)} \langle S_i^{\mu}(t) S_j^{\nu}(0) \rangle, \end{aligned} \quad (22)$$

where  $\mathbf{Q}$  is the momentum vector transfer, and  $f(\mathbf{Q})$  is the magnetic form factor of  $\text{Fe}^{2+}$ . Figure 3(b), and (e) show contour plots of  $I(\mathbf{Q}, \omega)$  calculated with the GLSWT along the  $[H, 0, 0.5]$ , and  $[H, H, 0.5]$  direction, respectively. The Hamiltonian parameters (see set  $\mathcal{A}$  in Table I) are extracted by fitting the measured positions

of the quasi-particle peaks (Gaussian-fitted peak centers of the experimental data) at the ZC. The resulting model can reproduce the dispersion relation of the two transverse modes  $T_1$  and  $T_2$  along the  $[H, 0, 0.5]$  and  $[H, H, 0.5]$  directions (Fig. 3 (a),(d)). Noticeably, the longitudinal mode closely reproduces the dispersion of the observed ‘ $L$ ’-mode. However, the GLSWT cannot reproduce the the broadening and renormalization of the longitudinal modes. Both effects arise from the decay of a longitudinal mode into two transverse modes that is induced by the cubic term  $\mathcal{H}^{(3)}$  of the expansion (9). To capture this effect we must then include the next order terms of the  $1/M$  expansion.

TABLE I. The parameters of the effective  $S = 1$  model extracted by fitting the Gaussian-peak centers of the experimental dispersion with the GLSWT and GLSWT + one loop calculated energies at the zone center  $\mathbf{Q}_m = (1, 0, 0.5)$ . In both cases, we assume  $\tilde{J}' = 0.1\tilde{J}$ , and  $\tilde{\Delta} = \tilde{\Delta}' = 1/3$ , i.e.  $\Delta = \Delta' = 1$  for the  $S = 2$  model (Heisenberg model without exchange anisotropy). The parameter set is referred to by its label ( $\mathcal{A}$  or  $\mathcal{B}$ ) in the text.

Theory	Label	$\tilde{J}$ (meV)	$\tilde{D}$ (meV)
GLSWT	$\mathcal{A}$	0.242	1.630
GLSWT + one-loop	$\mathcal{B}$	0.263	1.432

## V. NON-LINEAR CORRECTIONS

In this section we demonstrate that the generalization of the  $1/S$  expansion is simply a loop expansion. Based on this result, we compute the one-loop corrections to the linear theory presented in the previous section. As we explain in the next section, the one-loop correction accounts for both the broadening and the energy renormalization of the longitudinal mode near the zone center.

### A. Cubic Terms

After Fourier transforming and applying a Bogoliubov transformation, the cubic contributions to the generalized spin wave theory become

$$\mathcal{H}^{(3)} = \mathcal{H}_c^{(3)} + \mathcal{H}_l^{(3)}, \quad (23)$$

where

$$\begin{aligned} \mathcal{H}_c^{(3)} &= \frac{1}{\sqrt{N_s}} \sum_{\mathbf{q}_i} \sum_{\alpha_i=\pm 1} \delta(\mathbf{q}_1 + \mathbf{q}_2 + \mathbf{q}_3) \\ &\quad \left[ \frac{1}{3!} V_s^{(3)}(\mathbf{q}_{1,2,3}, \alpha_{1,2,3}) \beta_{\mathbf{q}_1, \alpha_1} \beta_{\mathbf{q}_2, \alpha_2} \beta_{\mathbf{q}_3, \alpha_3} + h.c. \right. \\ &\quad \left. + \frac{1}{2!} V_d^{(3)}(\mathbf{q}_{1,2,3}, \alpha_{1,2,3}) \beta_{\bar{\mathbf{q}}_1, \alpha_1}^\dagger \beta_{\bar{\mathbf{q}}_2, \alpha_2}^\dagger \beta_{\mathbf{q}_3, \alpha_3} + h.c. \right], \end{aligned} \quad (24)$$

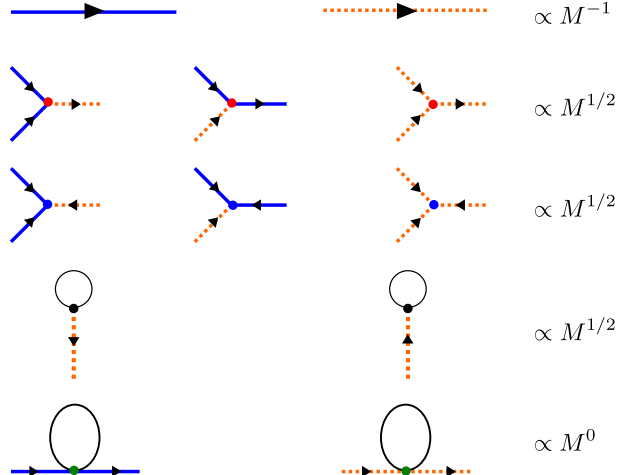


FIG. 5. Basic ingredients of the perturbative field theory in  $1/M$  for  $\text{Ba}_2\text{FeSi}_2\text{O}_7$ . Solid (dash) lines represent the bare propagator of the transverse (longitudinal) boson. The symmetry-allowed cubic vertices are shown on the second and third lines. The red (blue) dot represents a decay (sink) vertex. The cubic-linear vertices are listed on the fourth line. The last line represents the normal vertex  $V_{\alpha\alpha}^{(4,N)}$  from  $\mathcal{H}^{(4)}$ .

and

$$\begin{aligned} \mathcal{H}_l^{(3)} &= \frac{1}{\sqrt{N_s}} \sum_{\mathbf{q}} \sum_{\alpha=\pm 1} [V_l^{(3)}(\mathbf{q}, \mathbf{0}, \mathbf{q}; \alpha, -1, \alpha) \beta_{\mathbf{0}, -1}^\dagger + h.c.] \\ &= \sqrt{N_s} \sum_{\alpha=\pm 1} [V_{L,\alpha} \beta_{\mathbf{0}, -1}^\dagger + h.c.]. \end{aligned} \quad (25)$$

Here  $V_d^{(3)}$  and  $V_s^{(3)}$  are the decay and sink vertices, respectively. The symmetry allowed cubic vertices are depicted in the second and third lines of Fig. 5. Note that, unlike the  $\text{SU}(2)$  case, collinear magnetic ordering does not preclude cubic terms in the expansion (9) of the generalized  $\text{SU}(N)$  spin wave theory with  $N > 2$ . For the  $\text{SU}(3)$  case under consideration, the residual  $\text{U}(1)$  symmetry only requires that the  $\tilde{b}_{+1}$  boson must appear an even number of times (e.g.,  $\tilde{b}_{+1}\tilde{b}_{+1}$  or  $\tilde{b}_{+1}^\dagger\tilde{b}_{+1}^\dagger$ ) in the cubic terms.  $\mathcal{H}_l^{(3)}$  is a linear term that originates from the normal-ordering of the cubic term. This term renormalizes the optimal value  $\theta$  that was obtained from the minimization of  $\mathcal{H}^{(0)}$ . The integral of  $V_l^{(3)}(\mathbf{q}; \alpha, -1)$  over the entire Brillouin zone is the so-called *cubic-linear* vertex, which is non-zero only for the longitudinal boson at the ordering wave vector  $\mathbf{q} = \mathbf{0}$  (in the twisted frame). The explicit forms of  $V_{d,s}^{(3)}$  and  $V_l^{(3)}$  are derived in Appendix.(F).

### B. One-loop corrections

In this section, we will construct a systematic perturbative field theory that is controlled by  $1/M$ . This

scheme can be applied to study anharmonicities starting from *any* generalized spin wave theory based on a Schwinger boson representation of the generators of  $SU(N)$ . The well-known  $1/S$  expansion will be recovered for the particular case  $N = 2$  and  $M = 2S$ . As we will demonstrate below, the  $1/M$  expansion is just a particular example of the loop expansion that is commonly used to describe spontaneous symmetry breaking in particle theory [30]. The connection is more evident after noticing that  $M$  becomes an overall prefactor of the rescaled Hamiltonian (9),  $\tilde{\mathcal{H}} = \tilde{\mathcal{H}}_{\text{eff}}/M$ , once we also rescale the bosonic fields according to  $\tilde{b}_{\mathbf{r},\nu} = \tilde{b}_{\mathbf{r},\nu}/\sqrt{M}$ . Since the original interaction vertices  $V^{(n)}$  ( $n \geq 3$ ) scale as  $V^{(n)} \sim (M)^{2-\frac{n}{2}}$ , all vertices of the rescaled Hamiltonian  $\tilde{\mathcal{H}}(\{\tilde{b}_{\mathbf{r},\nu}, \tilde{b}_{\mathbf{r},\nu}^\dagger\})$  become of order  $M$ , while the propagator is still of order  $1/M$ . Thus, the order  $p$  of a particular one-particle irreducible diagram is  $V - I$ , where  $V$  is the number of vertices and  $I$  is the number of internal lines (note that the frequency  $\omega$  is of order  $M^0$  because the quadratic contribution  $\langle \tilde{\mathcal{H}}^{(2)} \rangle$  is independent of  $M$ ). Since the number of loops is  $L = I - V + 1$ , [36] we obtain the desired result:  $p = 1 - L$ .

Let us rederive this result without rescaling the fields and the Hamiltonian. As we already mentioned, Eq. (9) tells us that the interaction vertices  $V^{(n)}$  ( $n \geq 3$ ) scale as  $V^{(n)} \sim (M)^{2-\frac{n}{2}}$ . The quasi-particle propagator

$$\mathcal{G}_{0,\alpha}(\mathbf{k}, i\omega) = (-i\omega + \omega_{\mathbf{k},\alpha})^{-1}, \quad \alpha = \pm 1 \quad (26)$$

where  $\omega$  is the Matsubara frequency, scales as  $\mathcal{G}_{0,\alpha}(k) \sim M^{-1}$  because  $\omega_{\mathbf{k},\alpha}$  is of order  $M$  [see Eq. (9)].

The *dressed* single-particle propagator is obtained from the Dyson equation,

$$\mathcal{G}^{-1}(\mathbf{k}, i\omega) = \mathcal{G}_0^{-1}(\mathbf{k}, i\omega) - \Sigma(\mathbf{k}, i\omega), \quad (27)$$

where  $\Sigma(\mathbf{k}, i\omega)$  is the single-particle self-energy. At a given order in  $M$ , the dressed propagator includes two external legs,  $L$  independent loops,  $I$  internal lines (bare propagators  $\mathcal{G}_0$ ) and  $V_n$  interaction vertices of the type  $V^{(n)}$ . After a summation over the Matsubara frequency  $\omega \sim M^1$ , each loop gives a contribution of order  $M^1$ . Hence, the order  $p$  of a particular one-particle irreducible diagram contributing to  $\Sigma(\mathbf{k}, i\omega)$  is

$$p = L - I + \sum_{n \geq 3} V_n \left[ 2 - \frac{n}{2} \right]. \quad (28)$$

Since each internal line connects a pair of vertices, we have

$$\sum_{n \geq 3} n V_n = 2I + 2, \quad (29)$$

where  $\sum_{n \geq 3} n V_n$  is the total number of lines. Furthermore, the number of loops is equal to the number of independent momentum integrals. From the conservation of momentum at each vertex, we have

$$L = I - \left( \sum_{n \geq 3} V_n - 1 \right). \quad (30)$$

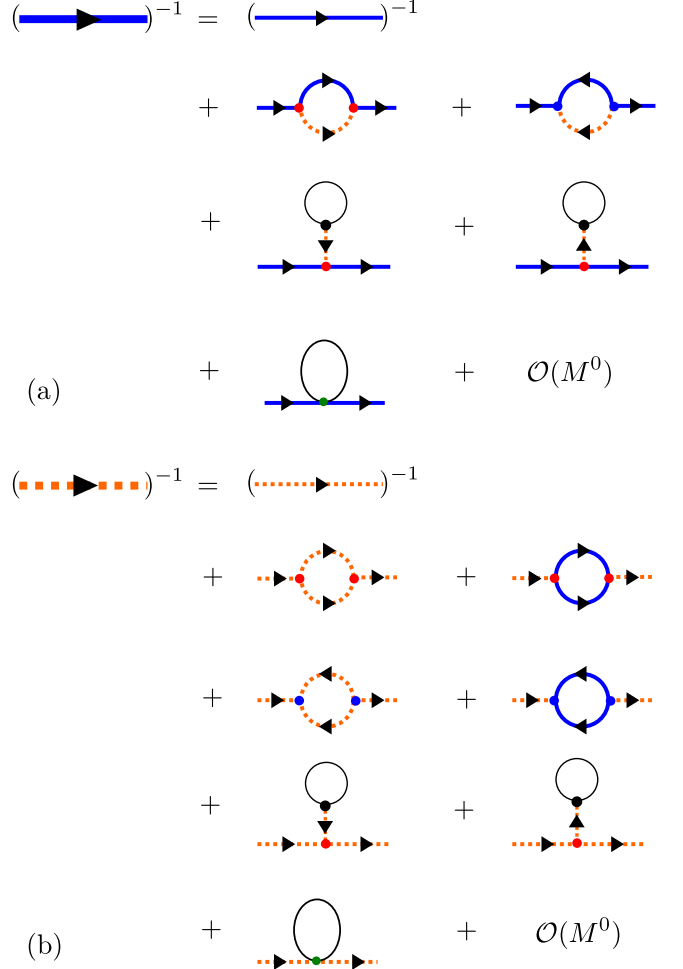


FIG. 6. Diagrammatic representation of the Dyson equation. (a) One-loop diagrams that contribute up to the order  $M^0$  for the transverse boson. (b) One-loop diagrams that contribute up to the order  $M^0$  for the longitudinal boson. The dressed propagator is denoted by a thick line, whereas the bare propagator is denoted by a thin line.

By combining the above results, we obtain

$$p = 1 + \sum_{n \geq 3} V_n - \sum_{n \geq 3} \frac{n V_n}{2} = 1 - L, \quad (31)$$

implying that the order of a given diagram is determined by the number of loops.

The lowest-order Feynman diagrams of order  $\mathcal{O}(M^0)$  are shown in Fig. 6. Since the inverse of the bare boson propagator is of order  $\mathcal{O}(M^1)$ , the remaining diagrams of order  $\mathcal{O}(M^0)$  give a relative  $1/M$  correction to the poles of the bare propagators. The real part of the new poles corresponds to the renormalized single-particle energy, whereas the imaginary part corresponds to the decay rate, which is responsible for the broadening of the quasi-particle peaks measured with INS.

The contributions to the self-energy from the decay

and from the source diagrams shown in Fig. 6 are

$$\Sigma_{\alpha}^d(\mathbf{q}, i\omega) = \frac{1}{2N_s} \sum_{\mathbf{k}, \alpha_1, \alpha_2 = \pm 1} \frac{|V_d^{(3)}(\bar{\mathbf{k}}, \mathbf{k} + \bar{\mathbf{q}}, \mathbf{q}; \alpha_1, \alpha_2, \alpha)|^2}{i\omega - \omega_{\mathbf{k}, \alpha_1} - \omega_{\mathbf{q} + \bar{\mathbf{k}}, \alpha_2}}, \quad (32)$$

and

$$\Sigma_{\alpha}^s(\mathbf{q}, i\omega) = -\frac{1}{2N_s} \sum_{\mathbf{k}, \alpha_1, \alpha_2 = \pm 1} \frac{|V_s^{(3)}(\mathbf{k}, \bar{\mathbf{k}} + \bar{\mathbf{q}}, \mathbf{q}; \alpha_1, \alpha_2, \alpha)|^2}{i\omega + \omega_{\mathbf{k}, \alpha_1} + \omega_{\mathbf{q} + \bar{\mathbf{k}}, \alpha_2}}, \quad (33)$$

respectively.

Finally, the diagrams that appear in the last line for both panels of Fig. 6 arise from the *normal ordering* of the quartic term  $\mathcal{H}^{(4)}$  in Eq. (9). These contributions simply renormalize the quadratic Hamiltonian:

$$\mathcal{H}_{NO}^{(4)} = \sum_{\mathbf{q}, \alpha, \alpha'} [V_{\alpha\alpha'}^{(4, N)} \beta_{\mathbf{q}, \alpha}^{\dagger} \beta_{\mathbf{q}, \alpha'} + (V_{\alpha\alpha'}^{(4, A)} \beta_{-\mathbf{q}, \alpha} \beta_{\mathbf{q}, \alpha'} + h.c.)], \quad (34)$$

where  $V_{\alpha\alpha'}^{(4, N)}(V_{\alpha\alpha'}^{(4, A)})$  represents the normal (anomalous) contributions. Since  $\mathcal{H}_{NO}^{(4)}$  is of order  $M^0$ , only the diagonal normal contribution arising from the normal vertex  $V_{\alpha\alpha'}^{(4, N)} \delta_{\alpha, \alpha'}$  gives a relative correction of order  $1/M$  to the bare single-particle energy given in Eq. (21) (the anomalous terms in Eq. (34) give a relative correction contribution order  $1/M^2$ ). The derivation of  $V_{\alpha\alpha}^{(4, N)}$  is included in Appendix G.

We note the parallel between the decay, sink, and quartic diagrams that give the  $1/M$  correction to the single-particle self-energy and the ones that appear in the  $1/S$  expansion of the standard SU(2) spin wave theory of *non-collinear* Heisenberg magnets [11]. The main difference is that the SU(3) theory includes an extra bosonic flavor that enables more symmetry-allowed decay channels. In addition, the cubic-linear diagram exists even in absence of magnetic field because the magnitude of the ordered magnetic moment can be renormalized by changing the variational parameter  $\theta$ . These diagrams, shown in the third line of Fig. 6 (a) and the fourth line of Fig. 6 (b), are obtained by contracting one of the legs of the decay vertex with the cubic-linear vertex shown in Fig. 5. By using the Feynman rules, the cubic-linear diagrams are calculated as

$$\Sigma_{\alpha}^{cl}(\mathbf{q}) = -\frac{1}{\omega_{0, -1}} \left( [V_d^{(3)}(\mathbf{0}, \bar{\mathbf{q}}, \mathbf{q}; \alpha, -1, \alpha)]^* V_{L, \alpha} + h.c. \right). \quad (35)$$

By applying the analytic continuation  $\omega \pm i\delta^+ \rightarrow i\omega$  and adopting the so-called *on-shell* approximation  $\omega = \omega_{\mathbf{q}}$  for Eq. (32) and Eq. (33), the renormalized pole of the dressed propagator  $\mathcal{G}$  is calculated as  $\tilde{\omega}_{\mathbf{q}, \alpha} - i\tilde{\Gamma}_{\mathbf{q}, \alpha} = \omega_{\mathbf{q}, \alpha} + V_{\mathbf{q}, \alpha\alpha}^{(4, N)} + \Sigma_{\alpha}^{cl}(\mathbf{q}) + \Sigma_{\alpha}^s(\mathbf{q}, \omega_{\mathbf{q}, \alpha}) + \Sigma_{\alpha}^d(\mathbf{q}, \omega_{\mathbf{q}, \alpha})$ , where the imaginary part of the pole  $\tilde{\Gamma}_{\mathbf{q}, \alpha}$  arises from the decay term  $\Sigma_{\alpha}^d$ , that accounts for the observed broadening of the longitudinal mode in most regions of the BZ [see Fig. 3 (c)(f)] (the calculations are summarized in

Appendix I and [37]). Moreover, the shift in the real part of the pole implies a corresponding renormalization in the model parameters. By fitting the neutron scattering data with the renormalized dispersion,  $\tilde{\omega}_{\mathbf{q}, \alpha}$ , we obtain a new set of optimal Hamiltonian parameters listed as set  $\mathcal{B}$  in Table I. It is interesting to note the significant change in  $r \equiv \tilde{D}/\tilde{J}$ , cf.  $r_{\text{GLSWT}} = 6.74$ , and  $r_{\text{GLSWT+one loop}} = 5.44$ . This change is a direct consequence of the substantial renormalization of the energy  $\omega_L(\mathbf{Q}_m)$  of the longitudinal mode at the magnetic zone center. In fact, an accurate calculation that goes beyond the one-loop approximation estimates that the critical  $\tilde{D}$  required to close the gap  $\omega_L(\mathbf{Q}_m)$  for  $\tilde{J}' = 0.1\tilde{J}$ , and  $\tilde{\Delta} = \tilde{\Delta}' = 1/3$  is around  $6.35\tilde{J}$  [38]. In other words, the Hamiltonian parameters extracted from fitting the experiment with the GLSW theory ( $\tilde{D} = 6.74\tilde{J}$ ) place  $\text{Ba}_2\text{FeSi}_2\text{O}_7$  on the quantum paramagnetic side of the phase diagram shown in Fig. 1, which obviously contradicts the experimental evidence.

## VI. COMPARISON BETWEEN EXPERIMENT AND THEORY

As can be seen in Fig. 3 and as discussed above, the set  $\mathcal{A}$  of Hamiltonian parameters extracted with the GLSWT is qualitatively incorrect. Hence in this section, we present a detailed comparison between the INS data and the theoretical results using the set  $\mathcal{B}$  presented in Table I.

Figures 7(a) and (b) show the quasi-particle dispersions along the  $[H, 0, 0.5]$  direction calculated with the GLSWT and GLSWT plus one-loop corrections compared to the measured dispersion. Near the ZC,  $\mathbf{Q}_m = (1, 0, 0.5)$ , the energies of longitudinal mode obtained from the GLSWT are noticeably higher than the peak centers of the measured ‘L’-mode (orange dots). The discrepancy in the dispersion is resolved by introducing the one-loop corrections. As discussed in Sec. VB, the sum of the real part of the one-loop diagrams renormalizes the energies of the longitudinal mode, leading to a better agreement with the observed peak positions near the ZC. At the same time, the sum of the imaginary part of the decay diagrams  $\Sigma_{\alpha}^d$  introduces intrinsic line-broadening to the longitudinal mode that is missing in the GLSWT. In Fig. 7 (b) and (d), the lower (upper) boundary of the red-shaded region is given by  $\tilde{\omega}_{\mathbf{k}, -1}(\mp) \tilde{\Gamma}_{\mathbf{k}, -1}$ , representing theoretical line-broadening of the longitudinal mode that is compared against the experimental FWHM (orange error bars). In particular, the above mentioned effects are most striking at  $\mathbf{Q}_m = (1, 0, 0.5)$ , therefore we present a comparison of the intensity line-cut at this momentum transfer in Fig. 7 (e). It is interesting to notice that the energy shift of the transverse mode is also captured by the one-loop corrections.

After verifying that the one-loop corrections can simultaneously capture the broadening of the longitudinal mode and the energy shift of both the transverse and the

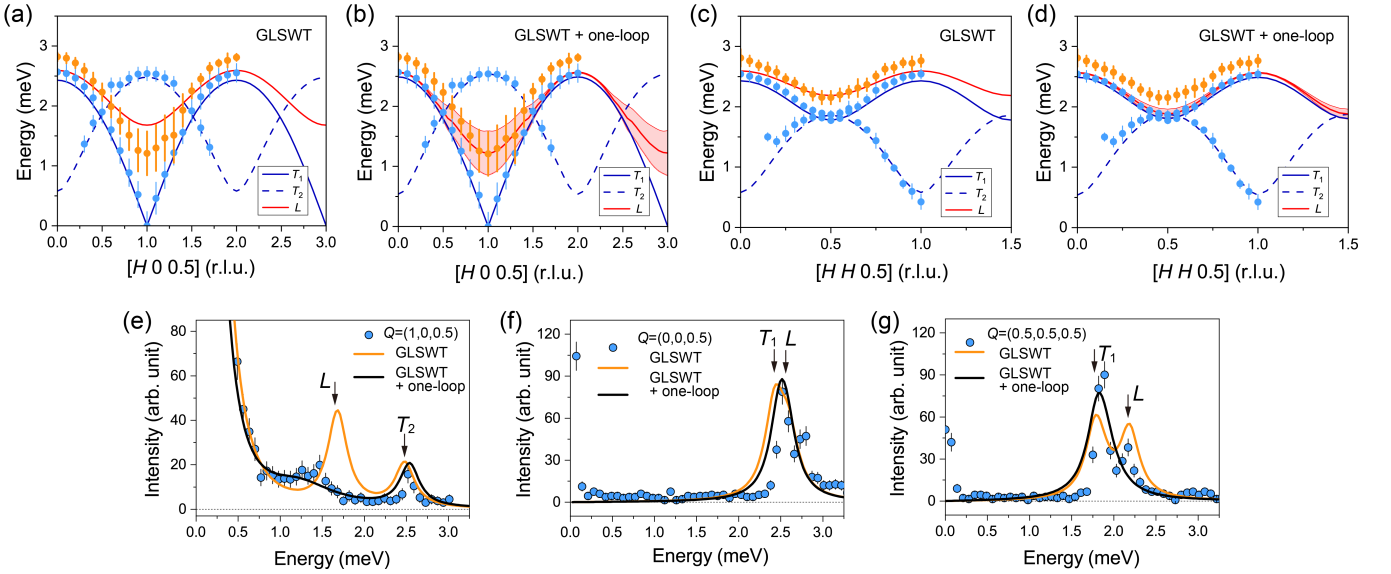


FIG. 7. Comparison of the measured and calculated dispersion along the  $[H, 0, 0.5]$  ((a), (b)) and  $[H, H, 0.5]$  ((c), (d)) directions. In all panels of this figure, the theoretical results are obtained for the parameter set  $\mathcal{B}$  in Table I. (a)-(d) Blue and orange filled circles indicate the measured transverse and longitudinal modes, obtained from the Gaussian fitting to the data shown in Fig. 4 (a). Dots and error bars indicate peak centers and full width at half maxima (FWHM) of the observed modes, respectively. Lines indicate the calculated dispersions obtained from the GLSWT and GLSWT+one-loop corrections. The red shaded region in (b) and (d) depict the decay (line-broadening) of the longitudinal mode given by the one-loop corrections. (e)-(g) Comparison between the measured (blue dots) and calculated (orange and black lines) INS intensities at three high-symmetric  $Q$ -points at  $(1, 0, 0.5)$ ,  $(0, 0, 0.5)$ , and  $(0.5, 0.5, 0.5)$ . All the experimental data were measured using CTAX with fixed  $E_f=3$  meV. For GLSWT, two transverse and longitudinal modes are denoted with  $T_1$ ,  $T_2$ , and  $L$ .

longitudinal modes at the magnetic ZC, it is natural to ask if this also holds true far away from the ZC. Figure 7 (f), (g) are the intensity cuts for two representative points on the ZB. At a first glance, the peak centers of both modes are reasonably reproduced by the one-loop corrections. A more detailed analysis reveals that the experimental FWHM of both peaks is equal to the instrumental resolution. However, as illustrated in Fig. 8 (a), since the longitudinal modes are still inside the two-magnon continuum, the one-loop correction predicts an intrinsic broadening (black curves) in Fig. 7 (f), (g).

To understand the origin of this discrepancy, we trace back the decay channel of the longitudinal mode on the zone boundaries. The two-magnon continuum at the zone edge starts at an energy equal to the sum of the single-magnon energies at the zone center and the zone boundary. Due to the U(1) symmetry of the effective Hamiltonian, the magnons are gapless at the zone center, implying that the onset of the two-magnon continuum coincides with the single magnon branch [see Fig. 8]. In absence of U(1) symmetry, the magnon modes become gapped and the longitudinal mode does not need to lie inside the two-magnon continuum for arbitrary values of the wave vector [see Fig. 8 (b)]. A small magnon gap pushes the onset of the two-magnon continuum to be above the energy of the longitudinal mode at the zone boundaries. This modification of the two-magnon spectrum precludes the decay of the longitudinal mode near

the zone boundary and explains the experimental observation. We then conjecture that the single-magnon dispersion is indeed gapped.

Unfortunately, it is difficult to extract the size of this gap from our INS data because of the large quasi-elastic component. Nevertheless, the simple analysis presented in Appendix C indicates that our data is indeed consistent with a finite spin gap. We note that the gap can only be captured by working with the original spin  $S=2$  Hamiltonian (1). The tetragonal symmetry allows for a single-ion anisotropy term of the form  $\mathcal{H}_A = A \sum_i [(S_i^x)^4 + (S_i^y)^4]$ , which breaks the global U(1) symmetry, generating a finite gap for the transverse mode. However, when we project the original  $S=2$  Hamiltonian onto the the low-energy space to obtain the effective spin  $S=1$  Hamiltonian (2), the term  $\mathcal{H}_A$  simply renormalizes the single-ion anisotropy, implying that the low-energy model acquires an “emergent” U(1) symmetry that is absent in the original high-energy model. Lastly, we note that the energies of the longitudinal mode on the zone boundaries after the one-loop corrections are slightly lower than the measured values. A simple analysis shows that a second nearest neighbor AFM interaction with  $\tilde{J}_2 \sim 0.2\tilde{J}$  can account for this discrepancy. For simplicity,  $\tilde{J}_2$  is not included in our calculation. Except for the discrepancy near the zone boundaries, the effective  $S=1$  model with one-loop corrections successfully captures most features of the INS data inside the BZ.

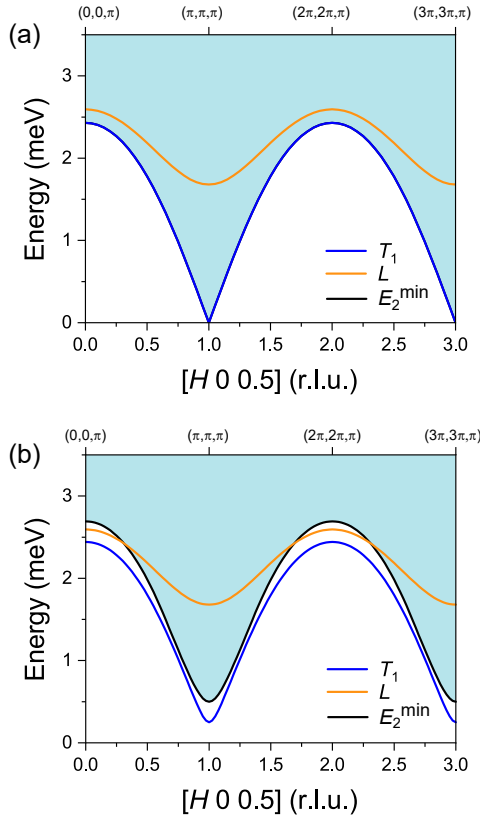


FIG. 8. Kinematic constraints for the decay of the longitudinal mode. The blue (orange) curve shows the calculated transverse (longitudinal) band dispersions along  $[H, 0, 0.5]$  with the GLSWT (using parameters set  $\mathcal{B}$  in Table I). The light blue-shaded areas indicate the two-transverse mode continuum, whose lower edge is indicated with a black solid line ( $E_2^{\min}$ ). (a) Results of the effective  $S = 1$  model. (b) Same as (a) but for a gapped branch of transverse modes (an ad hoc gap has been added to Eq. (21)).

Finally, we emphasize that the loop expansion preserves the Goldstone mode that results from the spontaneous breaking of the emergent  $U(1)$  symmetry group of  $\tilde{\mathcal{H}}_{\text{eff}}$ . More specifically, as it is shown in Appendix (H), the  $\mathcal{O}(M^0)$  correction to the real part of the self-energy vanishes for the Goldstone mode, although the *individual* contributions from the diagrams shown in Fig. 6 diverge as  $1/q$  in the long-wavelength limit. We note that previous attempts of computing the decay of the longitudinal mode [24] have not accounted for the renormalization of the single-particle dispersion arising from the  $1/M$  correction to the *real part* of the self-energy. This correction turns out to be relatively large for the case of  $\text{Ba}_2\text{FeSi}_2\text{O}_7$  and it becomes increasingly important upon approaching the quantum critical point that separates the magnetically ordered state from the QPM induced by a large enough value of the single-ion anisotropy  $D$ .

## VII. CONCLUSIONS

In summary,  $\text{Ba}_2\text{FeSi}_2\text{O}_7$  provides a natural realization of a quasi-2D easy-plane antiferromagnet in the proximity of the QCP that signals the transition into the QPM phase. Previous examples of low-dimensional easy-plane quantum magnets in the proximity of this QCP were typically on the quantum paramagnetic side of the quantum phase transition [25, 39–41].  $\text{Ba}_2\text{FeSi}_2\text{O}_7$  then allows us to study the strong decay and renormalization effects of the low-energy transverse and longitudinal modes of the AFM state. Furthermore, the distance to the  $O(2)$  QCP could be in principle controlled by chemical substitution, while the application of an in-plane magnetic field, that gaps out the transverse modes, can be used to control the decay rate of the longitudinal mode.

Here we have used the INS data of  $\text{Ba}_2\text{FeSi}_2\text{O}_7$  as a platform to test a loop expansion based on an  $SU(3)$  spin wave theory, [25, 26, 41, 42] that captures the longitudinal and the transverse modes at the linear level. This loop expansion, that generalizes the well-known  $1/S$  expansion of the  $SU(2)$  spin wave theory, allows us to reproduce the measured width and renormalization of the longitudinal and transverse modes near the zone center by just including a one-loop correction. Small discrepancies near the zone boundary are attributed to limitations of the effective low-energy  $S = 1$  model that we adopted for this work.

The loop expansion that we have described in this manuscript provides a general scheme for treating quantum magnets with more than one type of low-energy mode. In general, quantum magnets that exhibit low-energy modes with  $N - 1$  different “flavors” can be treated semi-classically using an  $SU(N)$  spin wave theory. The parameter of the semi-classical expansion is the number of loops in the Feynman diagrams that contribute to the single-particle propagator.

## ACKNOWLEDGMENTS

We thank Shang-Shun Zhang for useful discussions. This research was supported by the U.S. Department of Energy, Office of Science, Basic Energy Sciences, Materials Science and Engineering Division. This research used resources at the High Flux Isotope Reactor and Spallation Neutron Source, DOE Office of Science User Facilities operated by the Oak Ridge National Laboratory. The work at Max Planck POSTECH/Korea Research Initiative was supported by Nano Scale Optomaterials and Complex Phase Materials (2016K1A4A4A01922028), through the National Research Foundation (NRF) funded by MSIP of Korea. The work at Rutgers University was supported by the DOE under Grant No. DOE: DE-FG02-07ER46382.

## Appendix A: Experimental details

A single crystal of  $\text{Ba}_2\text{FeSi}_2\text{O}_7$  was grown using a floating zone furnace. Detailed information on the crystal growth is provided in Ref. [32]. Inelastic neutron scattering measurements were performed using the cold neutron triple-axis spectrometer (CTAX) at the High Flux Isotope Reactor (HFIR) and the hybrid spectrometer (HYSPEC) at the Spallation Neutron Source (SNS) at Oak Ridge National Laboratory [34]. A 2.15 g single crystal was aligned with the  $(H, H, L)$  and  $(H, 0, L)$  in the horizontal scattering plane for CTAX and HYSPEC experiments. A liquid helium cryostat was used to control temperature. At CTAX, the initial neutron energy was selected using a PG (002) monochromator, and the final neutron energy was fixed to  $E_f = 3.0$  meV by a PG (002) analyzer. The horizontal collimation was guide-open- $40^\circ$ - $120^\circ$ , which provides an energy resolution with full width half maximum (FWHM)=0.1 and 0.18 meV for  $\Delta E=0$  and 2.5 meV, respectively. For the HYSPEC experiment,  $E_i=9$  meV and a Fermi chopper frequency of 300 Hz were used, which provides an energy resolution of FWHM=0.28 meV and 0.19 meV at  $\Delta E=0$  and 2.5 meV, respectively. Measurements were performed at  $T=1.6$  K and 90 K by rotating the sample from  $-50^\circ$  to  $170^\circ$  with  $1^\circ$  steps. Data was symmetrized over positive and negative  $H$  and integrated over  $K=[-0.1, 0.1]$  and  $L=[0.4, 0.6]$ . In Fig. 3(a), there appears to be quasi-elastic scattering below 0.5 meV in low  $Q$ -region is attributed. This scattering arises from the incompletely blocked direct beam due to the oscillating collimator. All of data sets were reduced and analyzed using MANTID [43] and DAVE [44].

## Appendix B: Single-ion state of $\text{Fe}^{2+}$ in $\text{Ba}_2\text{FeSi}_2\text{O}_7$

Recent terahertz spectroscopy and X-ray absorption spectroscopy (XAS) on  $\text{A}_2\text{FeSi}_2\text{O}_7$  ( $\text{A}=\text{Sr}$  and  $\text{Ba}$ ) revealed that the considerable tetragonal distortion of  $\text{FeO}_4$ -tetrahedra (Sr: 17% and Ba: 26%  $z$ -compression from cubic) with large spin-orbit coupling of  $\text{Fe}^{2+}$  ( $\lambda \sim 20$  meV) induces significant easy-plane single-ion anisotropy in the system [32, 33]. Following the description for the spin-orbital states of  $\text{Fe}^{2+}$  in a tetrahedral environment, in  $\text{Ba}_2\text{FeSi}_2\text{O}_7$  the large single-ion anisotropy determines the ground state from the multiplet of  $\text{Fe}^{2+}$  ion. Starting with the free ion,  $^5D$  ( $L=2$ ,  $S=2$ ), the tetrahedral crystal field ( $\Delta_{Td}$ ) and tetragonal distortion ( $\delta_{Tetra}$ ) leave an A-manifold with 5 levels (see Fig. 9) with hybridized  $L^z$  and  $S^z$  states. When  $\Delta_{Td}, \delta_{Tetra} \gg \lambda$ , the orbital angular momentum is quenched, leading to a pure spin  $S=2$  quintet (see Fig 9 (a)). Introducing a single-ion term  $D(S^z)^2$  with easy-plane anisotropy, lifts the degeneracy of the quintet into levels with  $S^z=0$  (singlet),  $S^z = \pm 1$  (doublet), and  $S^z = \pm 2$  (doublet) where the energy-splitting between the states is given  $D$  and  $3D$ . Figure 9 (b) shows the inelastic neutron scattering measured at  $T=90$  K,  $\sim 7 * \Theta_{\text{CW}}$  (powder averaged Curie-

Weiss temperature  $\Theta_{\text{CW}}$  -12.8 K) where the single-ion physics dominates [32]. In the spectra, two flat excitations are visible at  $\text{d}E \sim 1.32$  meV and 3.9 meV which indicate transitions between levels as follows  $|S^z = 0\rangle \rightarrow |S^z = \pm 1\rangle$  and  $|S^z = \pm 1\rangle \rightarrow |S^z = \pm 2\rangle$ . Note that the transitions between  $|S^z = 0\rangle$  and  $|S^z = \pm 2\rangle$  are forbidden by dipole selection rules. At finite temperature, the thermal population of the spin states determines the effective spin of the system. In the low temperature region where  $T \ll 3 * D$  ( $\sim 45$  K), the  $|S^z = \pm 2\rangle$  states are depopulated and the system can then be treated as an effective  $S=1$ .

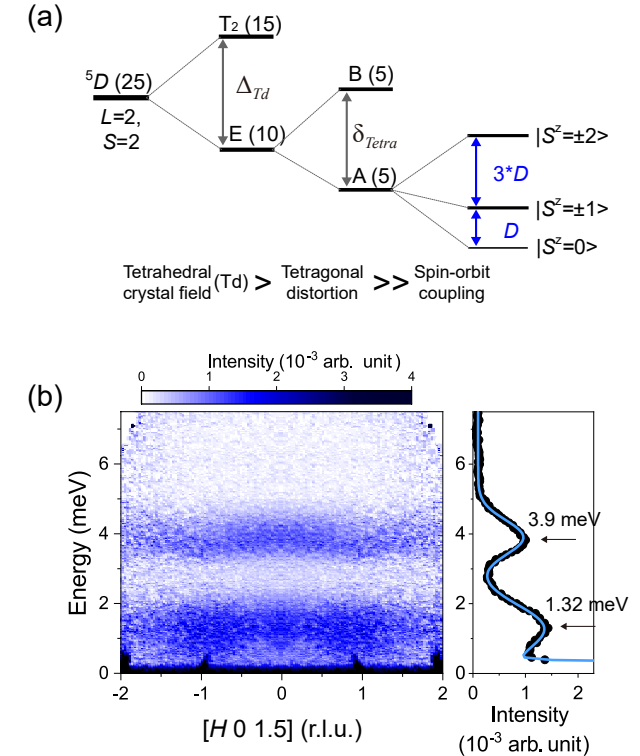


FIG. 9. (a) Orbital energy states of  $\text{Fe}^{2+}$  with a tetrahedral crystal field ( $\Delta_{Td}$ ), tetragonal distortion ( $\delta_{Tetra}$ ), and spin-orbit coupling ( $\lambda$ ). (b) The left panel shows inelastic neutron scattering data measured at  $T=90$  K, symmetrized over negative and positive  $H$  and integrated over  $L=[0.9, 2.1]$  and  $K=[-0.1, 0.1]$ . The integrated scattering intensity over  $H=[-2, 2]$  is shown in the right panel. The two peaks were fitted with Gaussian functions (solid blue line). Arrows indicate the peak centers at 1.32 meV and 3.9 meV.

## Appendix C: Analysis of a possible gap at magnetic zone center

To check for evidence of a gap in the spin wave dispersion near the ZC, the low energy inelastic neutron scattering was investigated using CTAX at HFIR with

$E_f=3$  meV. The energy resolution of the instrument (FWHM $\sim 0.101$  meV for elastic scattering), presents a challenge to directly extract a small gap due to the large scattering near the magnetic Bragg reflection at  $bmQ_m$ . As an alternative approach, we examine the spin wave dispersions near the ZC and compare the calculated spin wave dispersion with and without a small gap. The measured dispersion was obtained by fitting with resolution convoluted Gaussian function to constant momentum transfer scans for  $0.85 \leq H \leq 1.15$ . The extracted magnon dispersion is displayed as the contour plot along with the calculated spin waves with  $\Delta_{\text{gap}} = 0$  and 0.25 meV in in Fig. 10 (a). As shown, a gapless Goldstone mode ( $\Delta_{\text{gap}}=0$ ) has linear dispersion emanating from the ZC, whereas the gaped spin wave has quadratic dispersion near the ZC providing a possible means of distinguishing a gaped spectra from an gapless spectra. To find the best description of the dispersion near the ZC, the deviation between the data and calculated dispersion is defined as  $(E_{\text{exp.}} - E_{\text{calc.}})^2$ . The sum of this deviation is presented in Fig. 10 (b) as a function of the gap energy. The deviation has a minimum at  $\Delta_{\text{gap}} \sim 0.25$  meV, suggesting a gap in spin wave spectrum of  $\text{Ba}_2\text{FeSi}_2\text{O}_7$ .

#### Appendix D: Spin wave dispersion along $L$

Figure 11 shows INS data along the  $L$ -direction for  $[H, 0, L]$  with  $H=0$  and 1, measured using HYSPEC spectrometer. The spin excitations are weakly dispersing along  $L$  indicating quasi-two-dimensional behavior due to the relatively weak inter-layer coupling. As shown, the acoustic magnon ( $T_1$ ) has a bandwidth of 0.5 meV, and the  $T_2$  and  $L$  modes are almost completely flat along the  $L$  direction. The  $L$ -dependence of the spin excitations is reproduced by the GLSWT and GLSWT + one loop correction calculations with  $J'=J/10$ .

#### Appendix E: Generalized spin wave approach

In the local reference frame, the spin and quadrupolar operators can be expanded in  $1/M$  as:

$$\begin{aligned} S_{\mathbf{r}}^{\mu} &= M \tilde{S}_{00}^{\mu} + \sqrt{M} \sum_{\alpha=\pm 1} (\tilde{S}_{\alpha 0}^{\mu} b_{\mathbf{r}, \alpha}^{\dagger} + h.c.) \\ &+ \sum_{\alpha, \beta=\pm 1} (\tilde{S}_{\alpha \beta}^{\mu} - \tilde{S}_{00}^{\mu} \delta_{\alpha \beta}) \tilde{b}_{\mathbf{r}, \alpha}^{\dagger} \tilde{b}_{\mathbf{r}, \beta} \\ &- \frac{1}{2\sqrt{M}} \sum_{\alpha=\pm 1} \sum_{\beta=\pm 1} (\tilde{S}_{\alpha 0}^{\mu} \tilde{b}_{\mathbf{r}, \alpha}^{\dagger} \tilde{b}_{\mathbf{r}, \beta}^{\dagger} \tilde{b}_{\mathbf{r}, \beta} + h.c.) \\ &+ \mathcal{O}\left(\frac{1}{M^{3/2}}\right), \end{aligned} \quad (\text{E1})$$

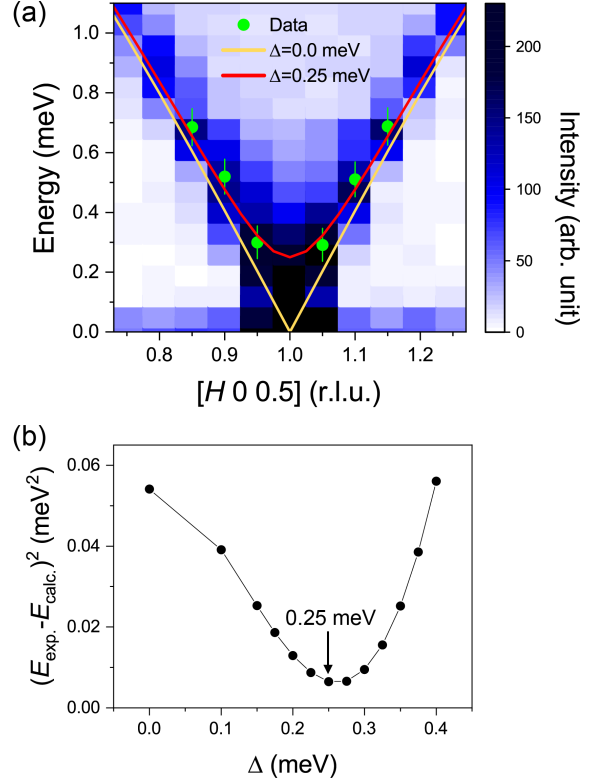


FIG. 10. (a) Contour map for low energy inelastic neutron scattering data near the zone center. The magnon dispersion extracted from the data is indicated by green circles and is compared with the dispersion calculated with the GLSWT with and without a gap ( $\Delta_{\text{gap}} = 0.25$  meV) in the spectrum. (b) Sum of the square of the energy difference between the measured and calculated dispersion as a function of gap size. The arrow marks the gap size  $\Delta_{\text{gap}} \sim 0.25$  meV that best fits the data.

$$\begin{aligned} (S_{\mathbf{r}}^z)^2 &= 1 - M \tilde{A}_{00} - \sqrt{M} \sum_{\alpha=\pm 1} (\tilde{A}_{\alpha 0} \tilde{b}_{\mathbf{r}, \alpha}^{\dagger} + h.c.) \\ &- \sum_{\alpha, \beta=\pm 1} (\tilde{A}_{\alpha \beta} - \tilde{A}_{00} \delta_{\alpha \beta}) \tilde{b}_{\mathbf{r}, \alpha}^{\dagger} \tilde{b}_{\mathbf{r}, \beta} \\ &+ \frac{1}{2\sqrt{M}} \sum_{\alpha=\pm 1} \sum_{\beta=\pm 1} (\tilde{A}_{\alpha 0} \tilde{b}_{\mathbf{r}, \alpha}^{\dagger} \tilde{b}_{\mathbf{r}, \beta}^{\dagger} \tilde{b}_{\mathbf{r}, \beta} + h.c.) \\ &+ \mathcal{O}\left(\frac{1}{M^{3/2}}\right). \end{aligned} \quad (\text{E2})$$

The expressions for the coefficients  $A_{\mathbf{k}, \alpha}$  and  $B_{\mathbf{k}, \alpha}$  of

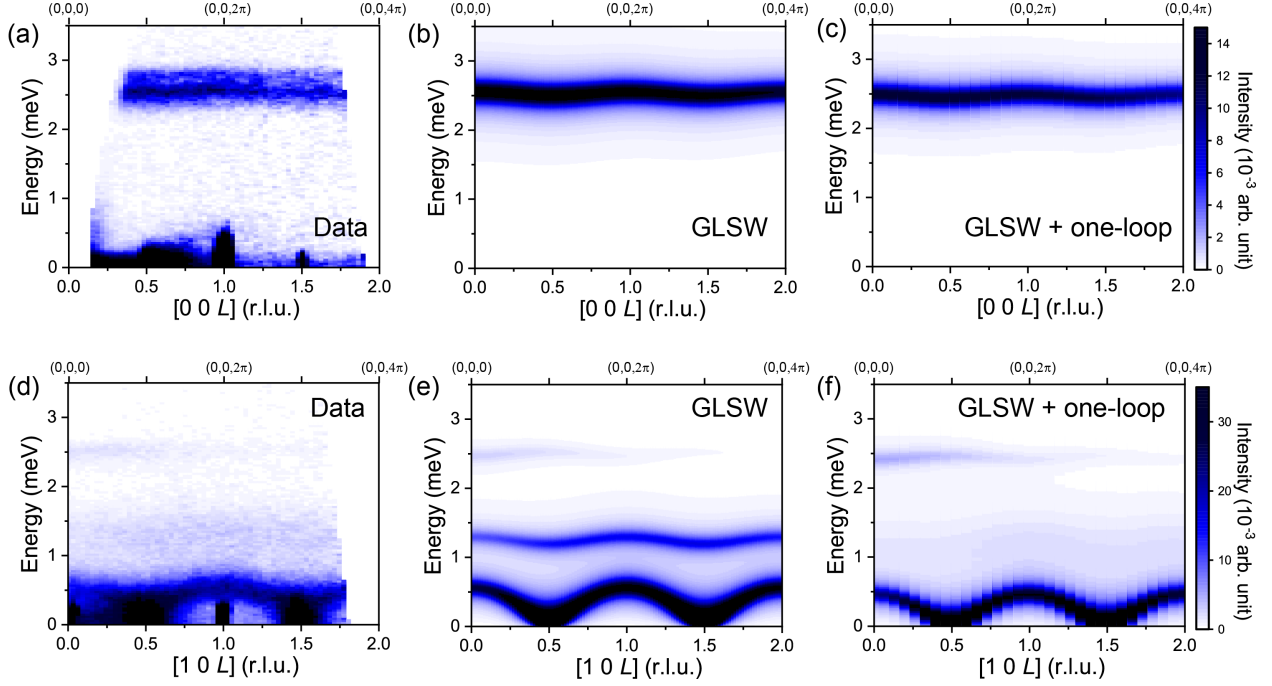


FIG. 11. Inelastic neutron scattering spectra along  $[H,0,L]$  for  $H=0$  and 1 along with the calculated spectra using the GLSWT and GLSWT+one loop corrections using parameter sets  $\mathcal{A}$  and  $\mathcal{B}$  in Table. I, respectively. All the calculated spectra were convoluted with the instrumental resolution of HYSPEC.

the quadratic Hamiltonian  $\mathcal{H}^{(2)}$  Eq. (17) are:

$$\begin{aligned}
 A_{\mathbf{k},+1} &= -8(x-1)x(2\tilde{J} + \tilde{J}') - (x-1)\tilde{D} \\
 &\quad + 2(x(1+\tilde{\Delta})-1)\tilde{J}\gamma_{\mathbf{k}}^{xy} \\
 &\quad + 2(x(1+\tilde{\Delta}')-1)\tilde{J}'\gamma_{\mathbf{k}}^z, \\
 B_{\mathbf{k},+1} &= -2(x(\tilde{\Delta}-1)+1)\tilde{J}\gamma_{\mathbf{k}}^{xy} \\
 &\quad - 2(x(\tilde{\Delta}'-1)+1)\tilde{J}'\gamma_{\mathbf{k}}^z, \\
 A_{\mathbf{k},-1} &= -16(x-1)x(2\tilde{J} + \tilde{J}') - (2x-1)\tilde{D} \\
 &\quad - 2(1-2x)^2(\tilde{J}\gamma_{\mathbf{k}}^{xy} + \tilde{J}'\gamma_{\mathbf{k}}^z), \\
 B_{\mathbf{k},-1} &= 2(1-2x)^2(\tilde{J}\gamma_{\mathbf{k}}^{xy} + \tilde{J}'\gamma_{\mathbf{k}}^z)
 \end{aligned} \tag{E3}$$

#### Appendix F: Cubic and cubic-linear vertices

In this section, we derive the cubic and cubic-linear vertices given in Eq. (24) and Eq. (25). The cubic Hamiltonian has three contributions

$$\mathcal{H}^{(3)} = \mathcal{H}_{\text{intra}}^{(3)} + \mathcal{H}_{\text{inter}}^{(3)} + \mathcal{H}_D^{(3)}, \tag{F1}$$

with

$$\begin{aligned}
 \mathcal{H}_{\text{intra}}^{(3)} &= \tilde{J} \sum_{\langle \mathbf{r}, \mathbf{r}' \rangle, \nu} \sum_{\alpha, \beta = \pm 1} \left\{ \sum_{\alpha' = \pm 1} a_{\nu} [2\tilde{\mathcal{S}}_{\alpha\beta}^{\nu} \tilde{\mathcal{S}}_{0\alpha'}^{\nu} \tilde{b}_{\mathbf{r}\alpha}^{\dagger} \tilde{b}_{\mathbf{r}\beta} \tilde{b}_{\mathbf{r}'\alpha'}] \right. \\
 &\quad \left. - a_{\nu} [\tilde{\mathcal{S}}_{0\alpha}^{\nu} \tilde{\mathcal{S}}_{00}^{\nu} (\tilde{b}_{\mathbf{r}\beta}^{\dagger} \tilde{b}_{\mathbf{r}\beta} \tilde{b}_{\mathbf{r}\alpha} + 2\tilde{b}_{\mathbf{r}'\beta}^{\dagger} \tilde{b}_{\mathbf{r}'\beta} \tilde{b}_{\mathbf{r}\alpha})] + h.c. \right\},
 \end{aligned}$$

$$\begin{aligned}
 \mathcal{H}_{\text{inter}}^{(3)} &= \tilde{J}' \sum_{\langle \mathbf{r}, \mathbf{r}' \rangle, \nu} \sum_{\alpha, \beta = \pm 1} \left\{ \sum_{\alpha' = \pm 1} b_{\nu} [2\tilde{\mathcal{S}}_{\alpha\beta}^{\nu} \tilde{\mathcal{S}}_{0\alpha'}^{\nu} \tilde{b}_{\mathbf{r}\alpha}^{\dagger} \tilde{b}_{\mathbf{r}\beta} \tilde{b}_{\mathbf{r}'\alpha'}] \right. \\
 &\quad \left. - b_{\nu} [\tilde{\mathcal{S}}_{0\alpha}^{\nu} \tilde{\mathcal{S}}_{00}^{\nu} (\tilde{b}_{\mathbf{r}\beta}^{\dagger} \tilde{b}_{\mathbf{r}\beta} \tilde{b}_{\mathbf{r}\alpha} + 2\tilde{b}_{\mathbf{r}'\beta}^{\dagger} \tilde{b}_{\mathbf{r}'\beta} \tilde{b}_{\mathbf{r}\alpha})] + h.c. \right\},
 \end{aligned}$$

$$\mathcal{H}_D^{(3)} = \frac{\tilde{D}}{2} \sum_{\mathbf{r}} \sum_{\alpha, \beta = \pm 1} [\tilde{A}_{0\alpha} \tilde{b}_{\mathbf{r}\beta}^{\dagger} \tilde{b}_{\mathbf{r}\beta} \tilde{b}_{\mathbf{r}\alpha} + h.c.],$$

To simplify the notation, we will write a particular term of (F1) (in momentum space) as (I) =  $\tilde{b}_{\bar{\mathbf{q}}_1, \alpha}^{\dagger} \tilde{b}_{\mathbf{q}_2, \beta} \tilde{b}_{\mathbf{q}_3, \gamma} f(\mathbf{q}_i, t)$ , with

$$f(\mathbf{q}_{1,2,3}, t) = \begin{cases} 1 & t = 0 \\ \gamma_{\mathbf{q}_3}^{xy} & t = 1 \\ \gamma_{\mathbf{q}_3}^z & t = 2 \end{cases}. \tag{F2}$$

The Nambu spinor of the bosonic operators can be Bogoliubov transformed into the quasi-particle representation  $\tilde{b}_{\mathbf{k}} = \mathcal{U}(\mathbf{k}) \tilde{\beta}_{\mathbf{k}}$ , where the matrix elements of  $\mathcal{U}(\mathbf{k})$  are obtained from the Bogoliubov coefficients given in Eq. (20)

$$\begin{aligned}
 \mathcal{U}(\mathbf{k}) &= \begin{pmatrix} \mathcal{U}_{2 \times 2}^{11}(\mathbf{k}) & \mathcal{U}_{2 \times 2}^{12}(\mathbf{k}) \\ \mathcal{U}_{2 \times 2}^{21}(\mathbf{k}) & \mathcal{U}_{2 \times 2}^{22}(\mathbf{k}) \end{pmatrix} \\
 &= \begin{pmatrix} u_{\mathbf{k},+1} & 0 & v_{\mathbf{k},+1} & 0 \\ 0 & u_{\mathbf{k},-1} & 0 & v_{\mathbf{k},-1} \\ v_{\mathbf{k},+1} & 0 & u_{\mathbf{k},+1} & 0 \\ 0 & v_{\mathbf{k},-1} & 0 & u_{\mathbf{k},-1} \end{pmatrix}.
 \end{aligned}$$

After applying the above-mentioned Bogoliubov transformation, we obtain

$$\begin{aligned}
 \text{(I)} = & \sum_{n_{1,2,3}} \left\{ F^{(a)}(\alpha\beta\gamma, n_{1,2,3}; \mathbf{q}_{1,2,3}, t) \beta_{\mathbf{q}_1, n_1} \beta_{\mathbf{q}_2, n_2} \beta_{\mathbf{q}_3, n_3} \right. \\
 & + F^{(b)}(\alpha\beta\gamma, n_{1,2,3}; \mathbf{q}_{1,2,3}, t) \beta_{\mathbf{q}_1, n_1}^\dagger \beta_{\mathbf{q}_2, n_2}^\dagger \beta_{\mathbf{q}_3, n_3}^\dagger \\
 & + F^{(c)}(\alpha\beta\gamma, n_{1,2,3}; \mathbf{q}_{1,2,3}, t) \beta_{\bar{\mathbf{q}}_1, n_1}^\dagger \beta_{\bar{\mathbf{q}}_2, n_2}^\dagger \beta_{\mathbf{q}_3, n_3} \\
 & + F^{(d)}(\alpha\beta\gamma, n_{1,2,3}; \mathbf{q}_{1,2,3}, t) \beta_{\bar{\mathbf{q}}_1, n_1}^\dagger \beta_{\mathbf{q}_2, n_2} \beta_{\mathbf{q}_3, n_3} \\
 & + L^{(c)}(\alpha\beta\gamma, n_{1,2,3}; \mathbf{q}_{1,2,3}, t) \delta_{\mathbf{q}_3, \bar{\mathbf{q}}_2} \delta_{n_3, n_2} \beta_{\bar{\mathbf{q}}_1, n_1}^\dagger \\
 & \left. + L^{(d)}(\alpha\beta\gamma, n_{1,2,3}; \mathbf{q}_{1,2,3}, t) \delta_{\mathbf{q}_2, \bar{\mathbf{q}}_1} \delta_{n_2, n_1} \beta_{\mathbf{q}_3, n_3} \right\}. \quad (\text{F3})
 \end{aligned}$$

The explicit forms of  $F^{(a,b,c,d)}$  and  $L^{(c,d)}$  can be obtained by simple algebras, which are not shown here for neatness.

The “sink” (“source”) function  $F^{(a)}$  ( $F^{(b)}$ ) is symmetric under permutations of all three legs (momenta and flavors). Consequently, we introduce the symmetrized functions

$$\tilde{F}^{(a)} \equiv \sum_{P(\mathbf{q}_{1,2,3}; n_{1,2,3})} F^{(a)}, \quad \tilde{F}^{(b)} \equiv \sum_{P(\mathbf{q}_{1,2,3}; n_{1,2,3})} F^{(b)}.$$

Similarly, the “decay” function  $F^{(c)}$  and the “fusion” function  $F^{(d)}$  are symmetrized for the two outgoing and the two incoming legs, respectively,

$$\tilde{F}^{(c)} = \sum_{P(\mathbf{q}_{1,2}; n_{1,2})} F^{(c)}, \quad \tilde{F}^{(d)} = \sum_{P(\mathbf{q}_{2,3}; n_{2,3})} F^{(c)}.$$

After inserting the above results into Eq. (F1), we obtain the explicit forms of the cubic vertices in  $V_{s/d}^{(3)}$  Eq. (24) and  $V_\alpha^L$  in Eq. (25).

## Appendix G: Quartic vertex

The quartic contributions to the expansion (9) are

$$\mathcal{H}^{(4)} = \mathcal{H}_{\text{intra}}^{(4)} + \mathcal{H}_{\text{inter}}^{(4)}, \quad (\text{G1})$$

with

$$\begin{aligned}
 \mathcal{H}_{\text{intra}}^{(4)} = & \tilde{J} \sum_{\langle \mathbf{r}, \mathbf{r}' \rangle, \nu} \sum_{\alpha, \beta = \pm 1} \left\{ [a_\nu \tilde{\mathcal{S}}_{00}^\nu \tilde{\mathcal{S}}_{00}^\nu \tilde{b}_{\mathbf{r}\alpha}^\dagger \tilde{b}_{\mathbf{r}'\beta}^\dagger \tilde{b}_{\mathbf{r}\alpha} \tilde{b}_{\mathbf{r}'\beta}] \right. \\
 & + \sum_{\alpha' \beta' = \pm 1} [a_\nu \tilde{\mathcal{S}}_{\alpha\beta}^\nu \tilde{\mathcal{S}}_{\alpha'\beta'}^\nu \tilde{b}_{\mathbf{r}\alpha}^\dagger \tilde{b}_{\mathbf{r}'\alpha'}^\dagger \tilde{b}_{\mathbf{r}\beta} \tilde{b}_{\mathbf{r}'\beta'}] \\
 & - 2 \sum_{\alpha' = \pm 1} [a_\nu \tilde{\mathcal{S}}_{\alpha\beta}^\nu \tilde{\mathcal{S}}_{00}^\nu \tilde{b}_{\mathbf{r}\alpha}^\dagger \tilde{b}_{\mathbf{r}'\alpha'}^\dagger \tilde{b}_{\mathbf{r}\beta} \tilde{b}_{\mathbf{r}'\alpha'}] \\
 & - \sum_{\alpha' = \pm 1} [a_\nu \tilde{\mathcal{S}}_{\alpha 0}^\nu \tilde{\mathcal{S}}_{\beta 0}^\nu \tilde{b}_{\mathbf{r}\alpha}^\dagger \tilde{b}_{\mathbf{r}'\beta}^\dagger \tilde{b}_{\mathbf{r}'\alpha'}^\dagger \tilde{b}_{\mathbf{r}\alpha'} + \text{h.c.}] \\
 & \left. - \sum_{\alpha' = \pm 1} [a_\nu \tilde{\mathcal{S}}_{\alpha 0}^\nu \tilde{\mathcal{S}}_{0\beta}^\nu \tilde{b}_{\mathbf{r}\alpha}^\dagger \tilde{b}_{\mathbf{r}'\alpha'}^\dagger \tilde{b}_{\mathbf{r}'\beta} \tilde{b}_{\mathbf{r}\beta'} + \text{h.c.}] \right\}.
 \end{aligned}$$

Similarly to the cubic contribution,  $\mathcal{H}_{\text{inter}}^{(4)}$  can be obtained from  $\mathcal{H}_{\text{intra}}^{(4)}$  by substituting  $\tilde{J} \rightarrow \tilde{J}'$ ,  $a_\nu \rightarrow b_\nu$ . The matrix elements appear in the normal ordering of the quartic vertex are defined as:

$$\begin{aligned}
 \bar{N}_{\mathbf{r}\mathbf{r}'}^{\alpha\beta} & \equiv \frac{1}{N} \sum_{\langle \mathbf{r}, \mathbf{r}' \rangle} \langle b_{\mathbf{r}\alpha}^\dagger b_{\mathbf{r}'\beta} \rangle \\
 & = \frac{1}{N} \sum_{\mathbf{k}} \sum_n \mathcal{U}_{\alpha, n}^{21}(\mathbf{k}) [\mathcal{U}_{\beta, n}^{21}(\mathbf{k})]^* \cos [\mathbf{k} \cdot (\mathbf{r}' - \mathbf{r})], \\
 \Delta_{\mathbf{r}\mathbf{r}'}^{\alpha\beta} & \equiv \frac{1}{N} \sum_{\langle \mathbf{r}, \mathbf{r}' \rangle} \langle b_{\mathbf{r}\alpha} b_{\mathbf{r}'\beta} \rangle \\
 & = \frac{1}{N} \sum_{\mathbf{k}} \sum_n \mathcal{U}_{\alpha, n}^{11}(\mathbf{k}) [\mathcal{U}_{\beta, n}^{21}(\mathbf{k})]^* \cos [\mathbf{k} \cdot (\mathbf{r}' - \mathbf{r})], \\
 \bar{\Delta}_{\mathbf{r}\mathbf{r}'}^{\alpha\beta} & \equiv \frac{1}{N} \sum_{\langle \mathbf{r}, \mathbf{r}' \rangle} \langle b_{\mathbf{r}\alpha}^\dagger b_{\mathbf{r}'\beta}^\dagger \rangle \\
 & = \frac{1}{N} \sum_{\mathbf{k}} \sum_n \mathcal{U}_{\alpha, n}^{21}(\mathbf{k}) [\mathcal{U}_{\beta, n}^{11}(\mathbf{k})]^* \cos [\mathbf{k} \cdot (\mathbf{r}' - \mathbf{r})],
 \end{aligned}$$

We note that some of these matrix elements are equal to zero because of the residual U(1) symmetry of the antiferromagnetic order. To obtain the normal-ordered Hamiltonian Eq. (34), we apply a mean-field (Hartree-Fock) decoupling to the quartic Hamiltonian Eq. (G1), for example,

$$\begin{aligned}
 & \tilde{b}_{\mathbf{r}\alpha}^\dagger \tilde{b}_{\mathbf{r}'\beta}^\dagger \tilde{b}_{\mathbf{r}\alpha} \tilde{b}_{\mathbf{r}'\beta} \\
 & \simeq \Delta_{\mathbf{r}\mathbf{r}'}^{\alpha\beta} \tilde{b}_{\mathbf{r}\alpha}^\dagger \tilde{b}_{\mathbf{r}'\beta}^\dagger + \bar{N}_{\mathbf{r}\mathbf{r}'}^{\beta\beta} \tilde{b}_{\mathbf{r}\alpha}^\dagger \tilde{b}_{\mathbf{r}\alpha} \\
 & + \bar{N}_{\mathbf{r}'\mathbf{r}'}^{\beta\alpha} \tilde{b}_{\mathbf{r}'\alpha}^\dagger \tilde{b}_{\mathbf{r}'\beta}^\dagger + \bar{\Delta}_{\mathbf{r}\mathbf{r}'}^{\alpha\beta} \tilde{b}_{\mathbf{r}\alpha} \tilde{b}_{\mathbf{r}'\beta} \\
 & + \bar{N}_{\mathbf{r}\mathbf{r}'}^{\alpha\alpha} \tilde{b}_{\mathbf{r}'\beta}^\dagger b_{\mathbf{r}'\beta} + \bar{N}_{\mathbf{r}\mathbf{r}'}^{\alpha\beta} \tilde{b}_{\mathbf{r}'\beta}^\dagger \tilde{b}_{\mathbf{r}\alpha}. \quad (\text{G2})
 \end{aligned}$$

The coefficients  $V_{\alpha\alpha}^{(4,N)}$  that appear in the normal term of Eq. (34) can be derived after consecutive Fourier and Bogoliubov transformations.

## Appendix H: One-loop diagrams in the long-wavelength limit

Without loss of generality, we consider an isotropic Heisenberg model, i.e.  $\tilde{J} = \tilde{J}'$ ,  $\tilde{\Delta} = \tilde{\Delta}'$  to show the  $1/\mathbf{q}$  divergence of the one-loop diagrams involving the Goldstone mode. According to Eq. (20),

$$\lim_{\mathbf{q} \rightarrow 0} u_{\mathbf{q},+}, v_{\mathbf{q},+} = \sqrt{\frac{\tilde{J}d}{v_{0,+}}} \frac{1}{\sqrt{\mathbf{q}}}, -\sqrt{\frac{\tilde{J}d}{v_{0,+}}} \frac{1}{\sqrt{\mathbf{q}}} \quad (\text{H1})$$

where  $v_{0,+} = 2\tilde{J}d\sqrt{\tilde{D}/(4\tilde{J}d^2) + 1/d}$  is the spin wave velocity of the Goldstone mode and  $d = 3$  is the spatial dimension of the lattice equal to half of the coordination number. Note that the cubic vertices are proportional to a product of the Bogoliubov coefficients of three legs

$$V_{d,s}^{(3)} \propto u(v)_{\mathbf{q}_1, \alpha} u(v)_{\mathbf{q}_2, \beta} u(v)_{\mathbf{q}_3, \gamma}. \quad (\text{H2})$$

For the decay and sink diagrams shown on the second line of Fig. 6 (a), we can choose, for instance,  $\mathbf{q}_3 = \mathbf{q} \sim \mathbf{0}$ ,  $\gamma = +1$  to contract with the leg of the long-wavelength bosons. Consequently,

$$\Sigma^{(d,s)}(+)\sim|V_{d,s}^{(3)}(\mathbf{q}_{1,2},\mathbf{q};\alpha\beta+)|^2\sim(1/\sqrt{\mathbf{q}})^2\sim1/\mathbf{q}. \quad (\text{H3})$$

As for the cubic-linear diagrams, we need to choose two legs to contract with the long-wavelength boson, implying that

$$\Sigma^{(cl)}(+)\sim V_d^{(3)}(\mathbf{0},-\mathbf{q}\mathbf{q};-++)\sim1/\mathbf{q}. \quad (\text{H4})$$

Finally, notice that  $V_{++}^{(4,N)}\sim1/\mathbf{q}$  in the long-wavelength limit, because the quadratic forms of the transverse boson in Eq. (G2) after the Bogoliubov transformation are proportional to  $u(v)_{\mathbf{q},+1}u(v)_{\mathbf{q},+1}$ . By adding up all diagrams in  $\mathcal{O}(M^0)$ , we have verified that the coefficient of the  $1/\mathbf{q}$ -factor vanishes, implying that the Goldstone mode is preserved after the one-loop correction.

## Appendix I: Calculation of the neutron intensity

The imaginary-time dynamical spin susceptibility is defined as:

$$\chi^{\mu\nu}(\mathbf{q},i\omega_n)=-\int_0^\beta d\tau e^{i\omega_n\tau}\langle\mathcal{T}_\tau[S_q^\mu(\tau)S_{\bar{q}}^\nu(0)]\rangle. \quad (\text{I1})$$

The *real-time* spin-spin correlation function in Eq. (22) is obtained by using the fluctuation-dissipation theorem at  $T=0$  after the analytic continuation  $i\omega_n\rightarrow\omega+i0^+$ :

$$S^{\mu\nu}(\mathbf{q},\omega)=-2\Im[\chi^{\mu\nu}(\mathbf{q},\omega)]. \quad (\text{I2})$$

Up to order  $\mathcal{O}(1/M)$ ,  $S^{\mu\nu}$  acquires two contributions:

$$S^{\mu\nu}=S_{\text{qp}}^{\mu\nu}+S_{\text{tc}}^{\mu\nu}, \quad (\text{I3})$$

where  $S_{\text{qp}}^{\mu\nu}$  includes contributions from the quasi-particle channel associated with “transverse fluctuations” of the SU(3) order parameter, while  $S_{\text{tc}}^{\mu\nu}$  includes two-particle contributions associated with “longitudinal fluctuations” of the SU(3) order parameter [37]. The latter is not analyzed in this work, as it only contributes to the continuum. After the one-loop corrections, the quasi-particle channel can be written as a linear combination of the dressed bosonic propagators  $\mathcal{G}$ . For details, see [37].

---

[1] L. Pitaevskii, Properties of the spectrum of elementary excitations near the disintegration threshold of the excitations, Sov. Phys. JETP **9**, 830 (1959).

[2] E. Lifshitz and L. Pitaevskii, Statistical Physics Part 2 (1980).

[3] A. D. B. Woods and R. A. Cowley, Structure and excitations of liquid helium, Reports on Progress in Physics **36**, 1135 (1973).

[4] M. B. Stone, I. A. Zaliznyak, T. Hong, C. L. Broholm, and D. H. Reich, Quasiparticle breakdown in a quantum spin liquid, Nature **440**, 187 (2006).

[5] T. Masuda, A. Zheludev, H. Manaka, L.-P. Regnault, J.-H. Chung, and Y. Qiu, Dynamics of Composite Haldane Spin Chains in IPA–CuCl<sub>3</sub>, Phys. Rev. Lett. **96**, 047210 (2006).

[6] J. Ma, Y. Kamiya, T. Hong, H. B. Cao, G. Ehlers, W. Tian, C. D. Batista, Z. L. Dun, H. D. Zhou, and M. Matsuda, Static and Dynamical Properties of the Spin-1/2 Equilateral Triangular-Lattice Antiferromagnet Ba<sub>3</sub>CoSb<sub>2</sub>O<sub>9</sub>, Phys. Rev. Lett. **116**, 087201 (2016).

[7] T. Hong, Y. Qiu, M. Matsumoto, D. A. Tennant, K. Coester, K. P. Schmidt, F. F. Awwadi, M. M. Turnbull, H. Agrawal, and A. L. Chernyshev, Field induced spontaneous quasiparticle decay and renormalization of quasiparticle dispersion in a quantum antiferromagnet, Nat. Commun. **8**, 15148 (2017).

[8] K. W. Plumb, K. Hwang, Y. Qiu, L. W. Harriger, G. E. Granroth, A. I. Kolesnikov, G. J. Shu, F. C. Chou, C. Rüegg, Y. B. Kim, and Y.-J. Kim, Quasiparticle-continuum level repulsion in a quantum magnet, Nat. Phys. **12**, 224 (2016).

[9] M. E. Zhitomirsky and A. L. Chernyshev, Colloquium: Spontaneous magnon decays, Rev. Mod. Phys. **85**, 219 (2013).

[10] T. Kim, K. Park, J. C. Leiner, and J.-G. Park, Hybridization and Decay of Magnetic Excitations in Two-Dimensional Triangular Lattice Antiferromagnets, J. Phys. Soc. Jpn. **88**, 081003 (2019).

[11] A. L. Chernyshev and M. E. Zhitomirsky, Spin waves in a triangular lattice antiferromagnet: Decays, spectrum renormalization, and singularities, Phys. Rev. B **79**, 144416 (2009).

[12] W. Zheng, J. O. Fjærstad, R. R. P. Singh, R. H. McKenzie, and R. Coldea, Anomalous excitation spectra of frustrated quantum antiferromagnets, Phys. Rev. Lett. **96**, 057201 (2006).

[13] P. Park, K. Park, T. Kim, Y. Kousaka, K. H. Lee, T. G. Perring, J. Jeong, U. Stuhr, J. Akimitsu, M. Kenzelmann, and J.-G. Park, Momentum-Dependent Magnon Lifetime in the Metallic Noncollinear Triangular Antiferromagnet CrB<sub>2</sub>, Phys. Rev. Lett. **125**, 027202 (2020).

[14] J. C. Leiner, T. Kim, K. Park, J. Oh, T. G. Perring, H. C. Walker, X. Xu, Y. Wang, S.-W. Cheong, and J.-G. Park, Magnetic excitations in the bulk multiferroic two-dimensional triangular lattice antiferromagnet (Lu, Sc)FeO<sub>3</sub>, Phys. Rev. B **98**, 134412 (2018).

[15] J. D. Thompson, P. A. McClarty, D. Prabhakaran, I. Cabrera, T. Guidi, and R. Coldea, Quasiparticle Breakdown and Spin Hamiltonian of the Frustrated Quantum Pyrochlore Yb<sub>2</sub>Ti<sub>2</sub>O<sub>7</sub> in a Magnetic Field, Phys. Rev. Lett. **119**, 057203 (2017).

[16] Y. Kamiya, L. Ge, T. Hong, Y. Qiu, D. Quintero-Castro,

Z. Lu, H. Cao, M. Matsuda, E. Choi, C. Batista, *et al.*, The nature of spin excitations in the one-third magnetization plateau phase of  $\text{Ba}_3\text{CoSb}_2\text{O}_9$ , *Nat. Commun.* **9**, 2666 (2018).

[17] D. Pekker and C. Varma, Amplitude/Higgs Modes in Condensed Matter Physics, *Annual Review of Condensed Matter Physics* **6**, 269 (2015).

[18] A. V. Chubukov, S. Sachdev, and J. Ye, Theory of two-dimensional quantum Heisenberg antiferromagnets with a nearly critical ground state, *Phys. Rev. B* **49**, 11919 (1994).

[19] S. Sachdev, Universal relaxational dynamics near two-dimensional quantum critical points, *Phys. Rev. B* **59**, 14054 (1999).

[20] D. Podolsky, A. Auerbach, and D. P. Arovas, Visibility of the amplitude (Higgs) mode in condensed matter, *Phys. Rev. B* **84**, 174522 (2011).

[21] D. Podolsky and S. Sachdev, Spectral functions of the Higgs mode near two-dimensional quantum critical points, *Phys. Rev. B* **86**, 054508 (2012).

[22] S. Gazit, D. Podolsky, and A. Auerbach, Fate of the Higgs Mode Near Quantum Criticality, *Phys. Rev. Lett.* **110**, 140401 (2013).

[23] F. Rose, F. Léonard, and N. Dupuis, Higgs amplitude mode in the vicinity of a  $(2+1)$ -dimensional quantum critical point: A nonperturbative renormalization-group approach, *Phys. Rev. B* **91**, 224501 (2015).

[24] A. Jain, M. Krautloher, J. Porras, G. H. Ryu, D. P. Chen, D. L. Abernathy, J. T. Park, A. Ivanov, J. Chaloupka, G. Khaliullin, B. Keimer, and B. J. Kim, Higgs mode and its decay in a two dimensional antiferromagnet, *Nat. Phys.* **13**, 633 (2017).

[25] Y. Kohama, A. V. Sologubenko, N. R. Dilley, V. S. Zapf, M. Jaime, J. A. Mydosh, A. Paduan-Filho, K. A. Al-Hassanieh, P. Sengupta, S. Gangadharaiah, A. L. Chernyshev, and C. D. Batista, Thermal Transport and Strong Mass Renormalization in  $\text{NiCl}_2\text{--}4\text{SC}(\text{NH}_2)_2$ , *Phys. Rev. Lett.* **106**, 037203 (2011).

[26] R. A. Muniz, Y. Kato, and C. D. Batista, Generalized spin-wave theory: Application to the bilinear-biquadratic model, *Prog. Theor. Exp. Phys.* **2014**, 083I01 (2014).

[27] Z. Zhang, K. Wierschem, I. Yap, Y. Kato, C. D. Batista, and P. Sengupta, Phase diagram and magnetic excitations of anisotropic spin-one magnets, *Phys. Rev. B* **87**, 174405 (2013).

[28] A. V. Chubukov, S. Sachdev, and T. Senthil, Large- $S$  expansion for quantum antiferromagnets on a triangular lattice, *Journal of Physics: Condensed Matter* **6**, 8891 (1994).

[29] O. A. Starykh, A. V. Chubukov, and A. G. Abanov, Flat spin-wave dispersion in a triangular antiferromagnet, *Phys. Rev. B* **74**, 180403(R) (2006).

[30] C. Sidney, *Aspects of Symmetry* (Cambridge, 1985).

[31] The linear spin-wave calculation overestimates the stability range of the magnetically ordered state.

[32] T.-H. Jang, S.-H. Do, M. Lee, V. Zapf, H. Wu, C. M. Brown, A. D. Christianson, S.-W. Cheong, and J.-H. Park, Two-dimensional square-lattice magnet  $\text{Ba}_2\text{FeSi}_2\text{O}_7$ : integer spin with large easy-plane single-ion anisotropy (in preparation).

[33] T. T. Mai, C. Svoboda, M. T. Warren, T.-H. Jang, J. Brangham, Y. H. Jeong, S.-W. Cheong, and R. Valdés Aguilar, Terahertz spin-orbital excitations in the paramagnetic state of multiferroic  $\text{Sr}_2\text{FeSi}_2\text{O}_7$ , *Phys. Rev. B* **94**, 224416 (2016).

[34] B. Winn, U. Filges, V. O. Garlea, M. Graves-Brook, M. Hagen, C. Jiang, M. Kenzelmann, L. Passell, S. M. Shapiro, X. Tong, and I. Zaliznyak, Recent progress on HYSPEC, and its polarization analysis capabilities, *EPJ Web of Conferences* **83**, 03017 (2015).

[35] J. Romhányi and K. Penc, Multiboson spin-wave theory for  $\text{Ba}_2\text{CoGe}_2\text{O}_7$ : A spin-3/2 easy-plane Néel antiferromagnet with strong single-ion anisotropy, *Phys. Rev. B* **86**, 174428 (2012).

[36] Every vertex introduces a delta function that reduces the number of independent momenta by one, except for one delta function that is left over for overall energy momentum conservation.

[37] M. Mourigal, W. T. Fuhrman, A. L. Chernyshev, and M. E. Zhitomirsky, Dynamical structure factor of the triangular-lattice antiferromagnet, *Phys. Rev. B* **88**, 094407 (2013).

[38] H. Zhang, and C. D. Batista, work in preparation.

[39] V. S. Zapf, D. Zocco, B. R. Hansen, M. Jaime, N. Harrison, C. D. Batista, M. Kenzelmann, C. Niedermayer, A. Lacerda, and A. Paduan-Filho, Bose-Einstein Condensation of  $S = 1$  Nickel Spin Degrees of Freedom in  $\text{NiCl}_2\text{--}4\text{SC}(\text{NH}_2)_2$ , *Phys. Rev. Lett.* **96**, 077204 (2006).

[40] S. A. Zvyagin, J. Wosnitza, C. D. Batista, M. Tsukamoto, N. Kawashima, J. Krzystek, V. S. Zapf, M. Jaime, N. F. Oliveira, and A. Paduan-Filho, Magnetic Excitations in the Spin-1 Anisotropic Heisenberg Antiferromagnetic Chain System  $\text{NiCl}_2\text{--}4\text{SC}(\text{NH}_2)_2$ , *Phys. Rev. Lett.* **98**, 047205 (2007).

[41] V. Zapf, M. Jaime, and C. D. Batista, Bose-Einstein condensation in quantum magnets, *Rev. Mod. Phys.* **86**, 563 (2014).

[42] M. Matsumoto, Electromagnon as a Probe of Higgs (Longitudinal) Mode in Collinear and Noncollinear Magnetically Ordered States, *J. Phys. Soc. Jpn.* **83**, 084704 (2014).

[43] Taylor, Jon, O. Arnold, J. Bilheux, A. Buts, S. Campbell, M. Doucet, and N. Draper, Mantid, A high performance framework for reduction and analysis of neutron scattering data, *Bulletin of the American Physical Society* **57** (2012).

[44] R. Azuah, L. Kneller, Y. Qiu, P. Tregenna-Piggott, C. Brown, J. Copley, and R. Dimeo, DAVE: A comprehensive software suite for the reduction, visualization, and analysis of low energy neutron spectroscopic data, *J. Res. Natl. Inst. Stan. Technol.* **114**, 341 (2009).